

Accepted by the Astronomical Journal on 7 July 1997

WFPC2 OBSERVATIONS OF THE CARINA DWARF SPHEROIDAL GALAXY¹

KENNETH J. MIGHELL²

Kitt Peak National Observatory³, National Optical Astronomy Observatories, P.O. Box 26732, Tucson,
AZ 85726-6732; Electronic mail: mighell@noao.edu

ABSTRACT

We present our analysis of *Hubble Space Telescope* Wide Field Planetary Camera 2 observations in F555W ($\sim V$) and F814W ($\sim I$) of the Carina dwarf spheroidal galaxy. The resulting V vs $V-I$ color-magnitude diagrams reach $V \approx 27.1$ mag. The reddening of Carina is estimated to be $E(V-I) = 0.08 \pm 0.02$ mag. A new estimate of the distance modulus of Carina, $(m-M)_0 = 19.87 \pm 0.11$ mag, has been derived primarily from existing photometry in the literature. The apparent distance moduli in V and I were determined to be $(m-M)_V = 20.05 \pm 0.11$ mag and $(m-M)_I = 19.98 \pm 0.12$ mag, respectively. These determinations assumed that Carina has a metallicity of $[\text{Fe}/\text{H}] = -1.9 \pm 0.2$ dex. This space-based observation, when combined with previous ground-based observations, is consistent with (but does not necessarily prove) the following star formation scenario. The Carina dwarf spheroidal galaxy formed its old stellar population in a short burst ($\lesssim 3$ Gyr) at about the same time the Milky Way formed its globular clusters. The dominant burst of intermediate-age star formation then began in the central region of the galaxy where stars formed for several billion years before the process of star formation became efficient enough in the outer regions of the galaxy to allow for the formation of large numbers of stars. There has been negligible star formation during the last few billion years. This observation provides evidence that at least some dwarf galaxies can have complex global star formation histories with local variations of the rate of star formation as a function of time and position within the galaxy.

¹ Based on observations made with the NASA/ESA *Hubble Space Telescope*, obtained from the data archive at the Space Telescope Science Institute, which is operated by the Association of Universities for Research in Astronomy, Inc. under NASA contract NAS5-26555.

² Guest User, Canadian Astronomy Data Center, which is operated by the Dominion Astrophysical Observatory for the National Research Council of Canada's Herzberg Institute of Astrophysics.

³ Kitt Peak National Observatory, National Optical Astronomy Observatories, is operated by the Association of Universities for Research in Astronomy, Inc. (AURA) under cooperative agreement with the National Science Foundation.

1. INTRODUCTION

Many of the Galactic dwarf spheroidal satellites have had complicated star formation histories with periods of star formation lasting many billions of years (e.g. Carina: Mighell 1990a, Mighell & Butcher 1992, Smecker-Hane *et al.* 1994, 1996; Fornax: Beauchamp *et al.* 1995; Leo I: Lee *et al.* 1993a; Leo II: Mighell & Rich 1996). These galaxies have a range of ages and/or metallicities despite their low stellar densities and escape velocities. Our current understanding of star formation suggests that the stars in dwarf spheroidal galaxies could not have formed at the currently observed low stellar densities. Faber & Lin (1983) suggested that the presence of a significant amount of dark matter is the key feature which distinguishes dwarf spheroidal galaxies from star clusters. Mateo *et al.* (1993) and Vogt *et al.* (1995) suggested that all small galaxies have similar and large dark-matter components. The Local Group dwarf spheroidal galaxies present a challenge to our current understanding of the formation and evolution of dwarf galaxies.

Precision photometry of crowded stellar fields seen in Local Group galaxies is very difficult even with the best ground-based new-technology telescopes. The high angular resolution of the *Hubble Space Telescope* Wide Field Planetary Camera 2 (WFPC2) instrument provides an excellent tool for the analysis of stellar populations in nearby Local Group galaxies. The WFPC2 instrument is now being used to make deep color-magnitude diagrams of a wide variety of stellar populations in Local Group galaxies. These deep color-magnitude diagrams are required for us to fully understand the star formation history and evolution of our neighboring galaxies in the Local Group.

In this work we extend our understanding of the complex star formation history of the Carina dwarf spheroidal galaxy using archival WFPC2 data. Section 2 is a discussion of the observations and photometric reductions. We review previous work Sec. 3 and present our results in Sec. 4. We summarize the results of the paper in Sec. 5. Appendix A describes how we revised the distance modulus for Carina primarily from existing data in the literature.

2. OBSERVATIONS AND DATA REDUCTION

The Carina dwarf spheroidal galaxy was observed with the *Hubble Space Telescope* Wide Field Planetary Camera 2 (WFPC2) on 1995 January 3 through the F555W ($\sim V$) and F814W ($\sim I$) filters. The WFPC2 WFALL aperture (Biretta *et al.* 1996) was centered on the target position of $\alpha = 06^{\text{h}} 41^{\text{m}} 49^{\text{s}}$ and $\delta = -50^{\circ} 58' 11''$ (J2000.0) and four low-gain observations were obtained: two 1100 s exposures in F814W (datasets U2LB0102T and U2LB0103T) and two 1100 s exposures in F555W (datasets: U2LB0105T and U2LB0106T). These observations were secured as part of the *HST* Cycle 4 program GTO/WFC 5637 and were placed in the public data archive at the Space Telescope Science Institute on 1996 January 3. The datasets were recalibrated at the Canadian Astronomy Data Centre on 1996 August 13 and were retrieved electronically that same

day. The cosmic rays were removed by using the **IRAF**⁴/**STSDAS** task **crrej** to make one clean F814W observation of 2200 s and one clean F555W observation of 2200 s. We only present the analysis of data obtained from the WF cameras in this paper.

Unsharp mask images of the clean F555W and F814W observations were made using the LPD (low-pass difference) digital filter which was designed by Mighell to optimize the detection of faint stars in *HST* WF/PC and WFPC2 images (Appendix A of Mighell & Rich 1995, and references therein). The two unsharp mask images were then added together to create a master unsharp mask image of each WF CCD. A simple peak detector algorithm was then used on the master unsharp images to create a list of point source candidates with coordinates $60 \leq x \leq 790$ and $60 \leq y \leq 790$ on each WF CCD. This allowed the use of almost the entire field-of-view of each WF camera while avoiding edge-effects in the outer regions.

The data were analyzed with the **CCDCAP** digital circular aperture photometry code developed by Mighell to analyze *HST* WF/PC and WFPC2 observations (Mighell *et al.* 1996, and references therein). A fixed aperture with a radius of 1.8 pixels was used for all stars on the WF CCDs. The local background level was determined from a robust estimate of the mean intensity value of all pixels between 1.8 and 6.0 pixels from the center of the circular stellar aperture. Point source candidates were rejected if either one of two criteria was satisfied: (1) the measured signal-to-noise ratio of either instrumental magnitude was less than 5; or (2) the center of the aperture [which was allowed to move in order to maximize the signal-to-noise ratio (*SNR*)] changed by more than 1 pixel from its detected position on the unsharp mask. Almost all photon noise spikes (due mainly to the background sky and diffraction spikes) were automatically eliminated by using these criteria.

Observed WFPC2 point spread functions (PSFs) vary significantly with wavelength, field position, and time (Holtzman *et al.* 1995a). There were not enough bright isolated stars in these WFPC2 observations to adequately measure the variation of the point spread function across each WF CCD using the observations themselves. We measured artificial point spread functions synthesized by the **Tiny Tim Version 4.0b** software package (Krist 1993, 1994) to determine the aperture corrections, Δ_r , required to convert instrumental magnitudes measured with an aperture of radius 1.8 pixels (0.18") to a standard aperture of radius 5.0 pixels (1" diameter). A catalog of 289 synthetic M-giant point spread functions was created with a 17×17 square grid for each filter (F814W and F555W) and CCD (WF2, WF3, and WF4). The spatial resolution of one synthetic PSF every 50 pixels in x and y allowed for the determination of aperture corrections for any star in the entire WFPC2 field-of-view to have a spatial resolution of $\lesssim 35$ pixels. The aperture corrections, by definition, are always negative. The average aperture corrections, $\langle \Delta_r \rangle$, are listed in Table 1.

⁴ IRAF is distributed by the National Optical Astronomy Observatories, which is operated by the Association of Universities for Research in Astronomy, Inc. under cooperative agreement with the National Science Foundation.

The WFPC2 point spread functions can vary with time due to spacecraft jitter during exposures and small focus changes caused by the *HST* expanding and contracting (“breathing”) once every orbit. These temporal variations of WFPC2 PSFs can cause small, but significant, systematic offsets in the photometric zeropoints when small apertures are used. Fortunately, these systematic offsets can be easily calibrated away by simply measuring bright isolated stars on each CCD twice: once with the small aperture and again with a larger aperture. The robust mean magnitude difference between the large and small apertures is then the zero-order aperture correction, δ_r , for the small aperture which, by definition, can be positive or negative. Zero-order aperture corrections are generally small for long exposures, however, they can be large for short exposures that were obtained while the WFPC2 was slightly out of focus (by a few microns) due to the expansion/contraction of the *HST* during its normal breathing cycle. The zero-order aperture corrections for these observations (δ_r : see Table 1) were computed using a large aperture with a radius of 5.0 pixels ($0.50''$) and a background annulus of $5.0 \leq r_{\text{sky}} \leq 8.0$ pixels.

The Charge Transfer Effect was removed from the instrumental magnitudes by using a 4% uniform wedge along the Y-axis of each WF chip as described in Holtzman *et al.* (1995b).

We used the standard WFPC2 color system (Holtzman *et al.* 1995b) which is defined using apertures $1''$ in diameter containing about 90% of the total flux from a star. The instrumental magnitudes, v_r and i_r , were transformed to Johnson V and Cousins I magnitudes using the following equations

$$\begin{aligned} V = & v_r + \Delta_r + \delta_r \\ & + \begin{bmatrix} -0.052 \\ \pm 0.007 \end{bmatrix} (V-I) + \begin{bmatrix} 0.027 \\ \pm 0.002 \end{bmatrix} (V-I)^2 + \begin{bmatrix} 21.725 \\ \pm 0.005 \end{bmatrix} \end{aligned} \quad (1)$$

and

$$\begin{aligned} I = & i_r + \Delta_r + \delta_r \\ & + \begin{bmatrix} -0.062 \\ \pm 0.009 \end{bmatrix} (V-I) + \begin{bmatrix} 0.025 \\ \pm 0.002 \end{bmatrix} (V-I)^2 + \begin{bmatrix} 20.839 \\ \pm 0.006 \end{bmatrix} \end{aligned} \quad (2)$$

where an instrumental magnitude of zero is defined as one DN/sec at the high gain state ($\sim 14 \text{ e}^-/\text{DN}$). The constants in brackets come from Table 7 of Holtzman *et al.* (1995b).

We present our stellar photometry of 3302 stars in the central region of the Carina dwarf spheroidal galaxy with $\text{SNR} \geq 5$ in both the F555W and F814W filters in the CD-ROM Table 1 found in the AAS CD-ROM Series, Vol. [XX], 199[X]. A printed version showing the first 20 stars is given in Table 2. The first column gives the identification (ID) of the star. The left-most digit of the ID gives the WFPC2 chip number (2, 3, or 4) where the star was found. The right-most 4 digits gives the x coordinate of the star multiplied by 10. The remaining 4 digits gives the y coordinate of the star multiplied by 10. All positions are given with respect to the U2LB0102T dataset. For example, the first star in Table 2 has an ID of 206092291 which indicates that it has the (x, y) position of (229.1, 60.9) on the WF2 CCD of the U2LB0102T dataset. The second and

third columns give the V magnitude and its r.m.s. photometric error σ_V . Likewise, the fourth and fifth columns give the $(V-I)$ color and its r.m.s. photometric error $\sigma_{(V-I)}$.

3. PREVIOUS STUDIES

The Carina dwarf spheroidal galaxy (Cannon *et al.* 1977) is one of the Galaxy’s nine dwarf spheroidal companions⁵, and it was the first of these in which an extended star formation history was conclusively detected.

Mould & Aaronson (1983) obtained a V vs $B - V$ color-magnitude diagram (CMD) of the Carina dwarf spheroidal galaxy that reached $V \approx 24$ mag and showed a main-sequence turnoff at $V_{\text{TO}} = 23.0 \pm 0.2$ mag. Carina was found to be metal-poor with a metallicity of $[\text{Fe}/\text{H}] = -1.9 \pm 0.2$ dex. A stubby, red horizontal branch (HB) was found at $V_{\text{HB}} = 20.5$ mag and a distance modulus of $(m - M)_0 = 19.8$ mag was derived by assuming an absolute V magnitude for the horizontal branch of $M_V^{\text{HB}} = 0.6$ mag. Isochrone fitting and a horizontal-branch to main-sequence turnoff difference of $\Delta V_{\text{TO}}^{\text{HB}} \approx 2.5$ mag yielded an age estimate of 7.5 ± 1.5 Gyr for the bulk of the stellar population of Carina.

Deep VR photometry ($V \leq 25.0$ mag) of Carina by Mighell (1990a) allowed him to produce a color-magnitude diagram that reached 2 mag below the main-sequence turnoff of the intermediate-age stellar population. This CMD showed the existence of the old stellar population suggested by the presence of RR Lyraes in the galaxy (Saha *et al.* 1986). Mighell estimated that the main-sequence turnoff magnitude of the old stellar population is $23.5 \leq V_{\text{TO}} \leq 23.8$ mag. While the stellar population of Carina is dominated by intermediate-age (6–9 Gyr) stars, Mighell found that 17 ± 4 percent of the total stellar population is older than 13 Gyr. From the analysis of the distribution of colors near the main-sequence turnoff, Mighell suggested that the old population in Carina was probably formed in a single burst lasting less than 3 Gyr and that the rate of star formation became negligibly small until the dominant intermediate-age population formed 6–9 Gyr ago.

Mighell (1990b) and Mighell & Butcher (1992) compared the deep V stellar luminosity function of Carina (Mighell 1990c) with theoretical stellar luminosity functions from *The Revised Yale Isochrones and Luminosity Functions* (Green *et al.* 1987, hereafter RYI) and a star formation history of Carina was derived that was fully consistent with star formation histories previously determined by analyzing color-magnitude diagrams.

Smecker-Hane *et al.* (1994) surveyed a large fraction of Carina and produced a shallow color-magnitude diagram ($V \leq 23.0$ mag) which shows a second, morphologically distinct, horizontal branch at $V_{\text{HB}} = 20.65 \pm 0.05$ mag. The fainter horizontal branch has blue and red HB

⁵ In order of discovery, the nine dSph companions of the Milky Way are Sculptor, Fornax, Leo I, Leo II, Ursa Minor, Draco, Carina, Sextans, and Sagittarius.

stars with an RR Lyrae strip; a morphology that is typical of old, metal-poor globular clusters. A distance modulus of $(m - M)_0 = 20.09 \pm 0.06$ for Carina was derived from the new determination of the apparent V magnitude of the horizontal branch and the I magnitude of the tip of the red giant branch ($I_{\text{TRGB}} = 16.15 \pm 0.05$ mag). Smecker-Hane *et al.* (1996) recently presented a preliminary deep R vs $B - R$ color-magnitude diagram ($R \leq 25.0$ mag) of Carina which clearly shows the intermediate-age and old stellar population turnoffs. This preliminary CMD also shows the presence of a small population of stars possibly as young as 2 Gyr old.

The simplest explanation of Carina’s complex horizontal branch morphology is that the stubby, red HB (at $V = 20.5$) is associated with its dominant intermediate-age stellar population and its fainter HB (at $V = 20.65 \pm 0.05$) is associated with its old stellar population. Mighell (1990a) showed that most of the stars in Carina belong to its intermediate-age (6–9 Gyr) stellar population and Smecker-Hane *et al.* (1994) report that $\sim 72\%$ of the HB stars are associated with the stubby, red HB. Theoretical horizontal branch models predict that the absolute V magnitude of the horizontal branch increases (fades) with age. Sarajedini *et al.* (1995), using the theoretical HB models of Lee *et al.* (1990, 1994), showed that the M_V^{HB} of a ~ 15 Gyr metal-poor ($[\text{Fe}/\text{H}] = -1.8$) stellar population is ~ 0.2 mag greater (fainter) than the M_V^{HB} of a ~ 7 Gyr stellar population with the same metallicity. This theoretical difference in the absolute V magnitude ($\Delta M_V^{\text{HB}} \approx 0.2$ mag) is quite close to the observed V magnitude difference found between Carina’s two horizontal branches ($\Delta V_{\text{HB}} \approx 0.15 \pm 0.05$ mag). If the faint HB is associated with Carina’s small old stellar population, then it is really not surprising that Mould & Aaronson (1983) and Mighell (1990a) did not detect the faint HB — the small field-of-view of their CCD observations prevented them from observing a statistically significant number of these rare stars.

Mighell’s (1990a) estimate that 17 ± 4 percent of the total stellar population is older than 13 Gyr should probably be interpreted as a *lower limit* of the size of Carina’s old stellar population since abundant intermediate-age stars near the main-sequence turnoff were compared with relatively rarer old subgiant branch stars. Mighell & Butcher (1992) found that the maximum size of Carina’s old stellar population is, conservatively, $40 \pm 5\%$ of the total stellar population. Smecker-Hane *et al.* (1994) found that the mean fraction of old horizontal branch stars in Carina is $27 \pm 7\%$ with no systematic radial dependence within 10 arcmin of the center of the galaxy. This value should probably be taken as an *upper limit* of the size of Carina’s old stellar population because the old HB stars live longer as horizontal branch stars than do the more massive intermediate-age HB stars. In support of these lower and upper limits, we note that the preliminary analysis of Smecker-Hane (1997) suggests that the old stellar population of Carina accounts for 20% (no error is given) of the stellar population.

Da Costa and Hatzidimitriou have obtained AAT spectra at the Ca II triplet (near 8600 Å: Armandroff & Da Costa 1991) of a sample of candidate Carina members (Da Costa 1993). Radial velocity measurements from the spectra confirmed that 15 stars were members of the Carina dwarf spheroidal galaxy. The mean abundance of the 15 member stars was $[\text{Fe}/\text{H}] = -1.88 \pm 0.08$ dex. There was one star, with $[\text{Fe}/\text{H}] = -2.32 \pm 0.10$, which is substantially more metal-poor

than the other 14 stars in the sample. The intrinsic abundance spread seen in the other 14 stars in the sample is small: $\sigma_{[\text{Fe}/\text{H}]} = 0.14$ dex. This spectroscopic metallicity determination agrees well with previous estimates based on color and magnitude differences derived from CCD stellar photometry of the red giant branch, horizontal branch and the main-sequence turnoff region of Carina ($[\text{Fe}/\text{H}] = -1.9 \pm 0.2$: Mould & Aaronson 1983; $[\text{Fe}/\text{H}] = -1.75 \pm 0.2$: Mighell 1990a; $[\text{Fe}/\text{H}] = -2.0$: Smecker-Hane *et al.* 1994). For the rest of this paper, we will assume that the metallicity of the Carina dwarf spheroidal galaxy is $[\text{Fe}/\text{H}] = -1.9 \pm 0.2$ dex.

4. THE CENTRAL REGION OF CARINA

The V vs $V-I$ color-magnitude diagram and apparent V stellar luminosity function of the observed stellar field in the Carina dwarf spheroidal galaxy are displayed in Fig. 1. This figure includes over 3,185 stars down to a limiting magnitude of $V \approx 27.1$ mag on the main sequence of Carina. The galactic latitude of Carina is low ($l = 260.1^\circ, b = 22.2^\circ$) and contamination by field stars can be substantial (e.g. Fig. 3 of Mould & Aaronson 1983; Fig. 2 of Smecker-Hane *et al.* 1994). The red giant branch in Fig. 1 is sparse and there is probably some contamination by field stars even though the field is located near the center of Carina [$r \approx 0.1r_c$ ⁶]. The clump of stars seen at $V \approx 20.5$ mag and $(V-I) \approx 0.9$ mag are helium core-burning stars belonging to the intermediate-age stellar population. The field-of-view of this observation (4.44 arcmin^2) is 3.79 times smaller than the field-of-view of Mighell (1990a) who found few, if any, horizontal branch stars belonging to the old stellar population of Carina. We would thus expect to find a statistically insignificant number of horizontal branch stars associated with the old stellar population of Carina in these WFPC2 observations.

Many stars of varying ages are seen in Fig. 1 to have evolved off the main-sequence. The width of the main-sequence turnoff region cannot be entirely due to photometric scatter because the turnoff region is significantly wider than the photometric errors at those magnitudes. Main sequences can be broadened by large spreads in metallicity, large variations in reddening, or long periods of star formation. Smecker-Hane *et al.* (1996) have estimated that the metallicity spread in Carina is small ($\lesssim 0.2$ dex) and we show in Appendix A that the reddening of central region of Carina is low [$E(V-I) = 0.08 \pm 0.02$ mag]. It is therefore unlikely that the observed width of the Carina main sequence is due to a metallicity spread or variations in reddening. Carina has been forming stars for many billions of years (Mighell 1990a), and thus the simplest explanation for Carina’s wide main sequence is that it is due to a long period of star formation.

Previous deep color-magnitude diagrams of Carina show a gap in the subgiant branch region redward of the main-sequence turnoff of the intermediate-age stellar population (Fig. 9 of Mighell

⁶ The core and tidal radii of Carina are $r_c = 8.8 \pm 1.2$ arcmin and $r_t = 28.8 \pm 3.6$ arcmin, respectively (Irwin & Hatzidimitriou 1995).

1990a, Fig. 1 of Smecker-Hane *et al.* 1996). Mighell (1990a) argued that this gap was due to negligible star formation between the bursts that created the old and intermediate-age populations. The gap seen in the deep color-magnitude diagram of Smecker-Hane *et al.* (1996) is not completely empty. This suggests that star formation might never have actually stopped between the two major bursts that created the old and intermediate-age stellar populations. However, some of the gap stars are undoubtedly foreground stars in the Milky Way. It is difficult to accurately determine the amount of Galactic field star contamination in a large survey of Carina without deep observations (hopefully of equal or greater areal coverage) of nearby fields well beyond the tidal radius of the galaxy.

The apparent V stellar luminosity function (SLF) of this WFPC2 observation of the central region of the Carina dwarf spheroidal galaxy is redisplayed in greater detail in Fig. 2. The shape of the faint end of the color-magnitude diagram in Fig. 1 is determined mainly by the requirement that the signal-to-noise ratio of each star must be at least 5 in both the F555W and F814W filters. The interpretive value of the apparent V SLF at magnitudes fainter than $V = 26.0$ mag will be limited by these selection effects. The open circles show the apparent V SLF for stars in the Fig. 1 CMD with the additional constraint that $\text{SNR} \geq 10$ in the F555W filter. The low-SNR and the high-SNR apparent V SLFs are identical in the magnitude range $19.8 \leq V \leq 26.0$ with the statistically insignificant difference in the $V = 25.7$ mag bin where the low-SNR SLF has one more star.

Figure 2 shows that the published completeness-corrected V stellar luminosity function of Mighell (1990c) is well matched by the apparent V stellar luminosity function of the WFPC2 field when it is scaled down by a factor of 3.2 to give the same number of stars in the V magnitude range $22.75 \leq V \leq 23.25$ which is the main-sequence turnoff region of the intermediate-age stellar population. The 6, 8, and 14 Gyr theoretical RYI stellar luminosity functions for $Z = 0.00025$ ($[\text{Fe}/\text{H}] = -1.9$ dex) and $Y = 0.24$ are displayed in Fig. 2 for comparative purposes. The apparent V WFPC2 Carina SLF appears to be well bracketed by the 6 and 8 Gyr RYI stellar luminosity functions in the magnitude range $22.5 \leq V \leq 25.0$ mag. This suggests that the *median* age of the *intermediate-age* stellar population in the central region of Carina is about 7 ± 1 Gyr on the RYI age scale.

Recent theoretical isochrones generally predict ages for Population II stars that are about 7–8% younger than the ages predicted by theoretical isochrones developed in the 1980’s (private communications: VandenBerg 1996, Demarque 1996, Chaboyer 1997). The younger ages are due principally to improvements of the input physics (e.g. the equation of state). A better estimate of the median age of the intermediate-age stellar population in the central region of Carina would thus be $\sim 6.5 \pm 0.9$ Gyr.

The V vs $V-I$ color-magnitude diagram of the main-sequence turnoff region of the Carina dwarf spheroidal galaxy is displayed in Fig. 3 with the theoretical RYI isochrones for the metallicity $Z = 0.00025$ ($[\text{Fe}/\text{H}] = -1.9$ dex) and helium abundance $Y = 0.24$. This figure suggests that the

bulk of star formation in the central region of Carina ended about 4 Gyr ago.

The main-sequence turnoff region is the most sensitive area of the color-magnitude diagram for the determination of the absolute age of stellar populations. Provided that the metallicity, apparent distance modulus and reddening of a star is known, one can determine the age of a subgiant branch star, in principle, by finding two isochrones that constrain the star in magnitude and color within the subgiant branch region. The age of the star can be estimated as being the average of the ages of the two isochrones with the estimate of the r.m.s. error being one half the difference in the ages of the two isochrones. Measurement (e.g. photometric) errors and systematic errors (e.g. uncertainties associated with the apparent distance modulus, reddening, and the physics and approximations of the stellar evolution model) will, of course, increase the uncertainty associated with the derived ages. This method of determining stellar ages can also be used to derive the star formation histories of simple stellar populations given high signal-to-noise stellar observations of systems that have experienced little or no chemical evolution.

The ages of subgiant branch stars in the central region of Carina were estimated in the following manner. The V vs $V-I$ color-magnitude diagram of the main-sequence turnoff region of the Carina dwarf spheroidal galaxy is displayed in Fig. 4 with the theoretical RYI isochrones for the metallicity $Z = 0.00025$ ($[\text{Fe}/\text{H}] = -1.9$ dex) and helium abundance $Y = 0.24$ at ages from 2 to 18 Gyrs in 1 Gyr increments (heavy solid curves, top to bottom). Isochrones were derived at 0.25 Gyr intervals from 2 to 18 Gyr by interpolating the standard RYI isochrones for $Z = 0.00025$ and $Y = 0.24$ at ages 2, 3, 4, \dots , 18 Gyr. These interpolated isochrones are displayed in Fig. 4 (light curves, top to bottom) from a point on the isochrone near the main-sequence turnoff⁷ to the base of the red giant branch which was defined as the place on the isochrone where the dereddened color $(V-I)_0$ is 0.70 mag. The initial age estimate, t'_{Gyr} , of each of the 152 stars within the bounded region of Fig. 4 is given in Table 3.

Better age estimates can be derived from Monte Carlo simulations using the photometric data given in CD-ROM Table 1. One thousand “observations” of each of the 152 stars in the bounded region of Fig. 4 were simulated (see Fig. 5) by using two-dimensional Gaussian distributions with mean V magnitudes and $V-I$ colors and standard deviations in V and $V-I$ defined as the respective measured values of V , $V-I$, σ_V , $\sigma_{(V-I)}$, which were given originally in CD-ROM Table 1 and duplicated in Table 3. The mean stellar age (in Gyr on the RYI age scale) and r.m.s. error for each of the 152 stars in the bounded region is given in Table 3 columns $\langle t_{\text{Gyr}} \rangle$ and $\sigma_{\langle t_{\text{Gyr}} \rangle}$, respectively. The mean stellar ages were determined by analyzing only the simulated observations that were found to be inside the bounded region.

The r.m.s. errors of the stellar age estimates increase with age (see Fig. 6) because the spacing between theoretical isochrones generally decreases with increasing age and photometric errors increase with apparent magnitude. The brightest subgiant branch star in the bounded region of

⁷ Defined as the location on the isochrone where the RYI equivalent evolutionary phase is EEP= 67.

Fig. 5 is star 256051426 which has an age estimate of 3.13 ± 0.14 Gyr. The small error estimate for this star is due to the fact that all of the 1000 simulated “observations” were found in the fifth age bin (5.00–5.25 Gyr). Star 317853886 is 1.289 ± 0.015 mag fainter and its 1000 simulated observations were spread across 4 bins which translates to an r.m.s. error of 0.29 Gyr for a mean stellar age of 9.54 Gyr on the RYI age scale. Stars fainter than $V \approx 23$ mag will increasingly suffer from “bin hopping” due primarily to color errors.

The mean estimated ages (in Gyr on the RYI age scale) and r.m.s. errors of all 152 stars in the bounded region of Fig. 4 are shown in Fig. 7. The r.m.s. errors increase with age, as expected, until the mean estimated age of ~ 15 Gyr. which occurs near the bottom of the bounded region. This region in Fig. 5 shows that many of the simulated observations are found outside of the bounded region, which suggests that mean estimated ages greater than ~ 15 Gyr are probably not reliable due to incompleteness effects.

How many stars in the bounded region actually belong there? While the vast majority of the simulated “observations” shown in in Fig. 5 are found within the bounded region, some of the stars are found beyond the edges of the bounded region. It is quite likely that some of the stars within the bounded region have been photometrically scattered *into* the bounded region. Unfortunately, it is impossible to precisely say which stars have done so without *a priori* knowledge of the stellar magnitudes and colors. We introduced the above Monte Carlo simulations so that we could obtain better stellar age estimates. We now reuse these same simulations in an attempt to determine just how many stars in the bounded region actually belong there.

A total of 11,104 simulated observations out of a grand total of 152,000 were found outside of the bounded region in Fig. 5. This suggests that probably no more than $\sim 92\%$ (~ 140) of the 152 stars found within the bounded region actually belong there. The recovery probabilities, p , of all 152 stars in the bounded region of Fig. 4 is given in Table 3. There are 77 stars in Table 3 which had all 1000 of their simulated observations found within the bounded region ($p \equiv 1$). Only 12 stars had fewer than 700 of their 1000 simulated observations found within the bounded region ($p < 0.700$). The recovery probabilities given in Table 3 are summarized in Table 4. This table shows that one star (225033399) had a recovery probability of $p = 0.897$. Of the 116 stars with recovery probabilities $p \geq 0.897$ (shown in Fig. 8) only 1105 simulated observations (out of a grand total of 116,000) were found outside of the bounded region. Table 4 also gives the total recovery probabilities, p' , which is defined as $p' \equiv \sum \text{in} / (\sum \text{in} + \sum \text{out})$ where $\sum \text{in}$ and $\sum \text{out}$ are given in Table 4. Using the example above, we see that $p' > 0.990$ for the the 116 stars with recovery probabilities $p \geq 0.897$. This implies that there is a 99% probability that these 116 stars actually belong inside the bounded region. In other words, only ~ 1 star out of the 116 probably does *not* belong within the bounded region.

The estimated mean stellar ages of the conservative subset of 116 subgiant branch stars ($p \geq 0.897 \Rightarrow p' \geq 0.990$) are displayed as the solid histogram at the bottom of Fig. 9. The median age of these 116 subgiant branch stars in the central region of Carina is ~ 6.9 Gyr (~ 7.5 Gyr on

the RYI age scale). This estimate agrees quite well with the estimate of $\sim 6.5 \pm 0.9$ Gyr for the median age of the intermediate-age stellar population which was derived above from the analysis of the apparent stellar luminosity function.

Any analysis of the high-resolution (0.25 Gyr bin width) star-count histogram at the bottom of Fig. 9 will be affected by small number (Poisson) statistics. This analysis uncertainty can be reduced by boosting the signal-to-noise ratio of the data at the cost of degrading the age resolution. Two 0.25 Gyr wide bins were added together to produce 2 low-resolution star-count histograms with 0.5 Gyr bin widths that are offset by one 0.25 Gyr bin from each (see Fig. 9): the vertical-shaded histogram gives the counts at 2.00, 2.50, 3.00, 3.50, ... Gyr; the horizontal-shaded histogram gives the counts at 2.25, 2.75, 3.25, 3.75, ... Gyr.

Small number statistics preclude the derivation of a detailed star formation history from the high-resolution star-count histogram at the bottom of Fig. 9. For example, a comparison of the data between 4 and 14 Gyr with a model which assumes 3 stars in every 0.25 Gyr bin shows that this simple star formation history can not be excluded at the 99% confidence level. The current dataset is thus fully consistent with the statement that the central region of Carina continuously formed stars between ~ 3.7 and ~ 13 Gyr ago (4–14 Gyr on the RYI age scale). There may well be some stars younger than ~ 3.7 Gyr but they are not detected in significant quantities. And even though there probably are stars present in this central region of Carina that belong to the old stellar population, little can be said about them due to their rarity and the various interpretation problems (e.g. incompleteness effects, large age uncertainties) shown above.

Mighell (1990a) suggested that the Carina dwarf spheroidal galaxy probably experienced a period of negligible stars formation between the old and intermediate-age stellar populations. This period was estimated to have lasted about 6–8 Gyr. The preliminary analysis of Smecker-Hane (1997) has suggested that Carina experienced a long quiescent period of star formation between 7 and 10 Gyr ago. Shifting from the LDZ distance scale (which was presumably used) to the CDKKS distance scale causes the distance modulus to be ~ 0.10 mag smaller at $[\text{Fe}/\text{H}] = -1.9$ dex (see Appendix A for more details). Decreasing the distance modulus by ~ 0.10 mag increases these ages by $\sim 9\%$ (e.g. Eq. 2 of Mighell & Butcher 1992) giving an approximate age range of 7.6–10.9 Gyr for the period of negligible star formation between the old and intermediate-age stellar populations of the Carina dwarf spheroidal galaxy.

Figure 8 shows that there are 27 stars ($\sim 23\%$ of 116 stars) between estimated mean RYI ages of 8.25 and 11.75 Gyr which is the comparable age range on the RYI age scale. Foreground stellar contamination in the subgiant branch region of the Carina color-magnitude diagram is probably quite negligible for the small field-of-view of the WFPC2 observations: $\lesssim 0.5$ foreground stars would be expected with colors $B - V < 1.0$ mag in the relevant magnitude range of $22.5 \leq V \leq 23.0$ (see Fig. 10 of Mighell 1990c).

These stars have r.m.s. errors of ~ 0.5 Gyr ($\sim 2 \times 0.25$ Gyr bins) which could cause some younger stars to be measured as being older because they were scattered into the given age range.

Similarly, some older stars could have been scattered into the given age range which would cause them to be measured too young. If we make the highly unlikely assumption that *all* of the stars within 0.5 Gyr of both ends of the age range were due to such scattering, then 20 stars would still remain with estimated mean ages between ~ 8.1 and ~ 10.4 Gyr ($8.75 \leq \langle t_{\text{Gyr}} \rangle < 11.25$ Gyr on the RYI age scale). This subset of 20 stars is a significant fraction (17%) of the total set of 116 subgiants that have a 99% probability of being found within the bounded region of Fig. 4. The central region of Carina apparently was forming stars during the multi-billion year “global” star-formation gap between the old and intermediate-age stellar populations of Carina which was previously found in ground-based studies. This observation is then consistent with the interpretation that the intermediate-age burst of star formation in Carina began in the central region of the galaxy and proceeded there for many billions of years before it occurred in the outer regions of the galaxy as observed in previous ground-based studies.

This space-based observation, when combined with previous ground-based observations, is consistent with (but does not necessarily prove) the following star formation scenario. The Carina dwarf spheroidal galaxy formed its old stellar population in a short burst ($\lesssim 3$ Gyr) at about the same time the Milky Way formed its globular clusters. The dominant burst of intermediate-age star formation then began in the central region of the galaxy where stars formed for several billion years before the process of star formation became efficient enough in the outer regions of the galaxy to allow for the formation of large numbers of stars. Ground-based color-magnitude diagrams clearly show a gap in the subgiant branch region between the old and the dominant intermediate-age stellar populations. The very existence of this gap allowed Mighell (1990a) to make the first estimate of the size and age of Carina’s old stellar population. If old intermediate-age (~ 8 – 11 Gyr old) stars *had* formed in the outer regions *in significant numbers*, then the gap would not exist because the subgiant branch region of the color-magnitude diagram would be filled with evolved stars. However, the gap *does* exist and that strongly suggests that the old intermediate-age stars preferentially formed in the central region of the galaxy.

Analysis of WFPC2 observations of the And I dwarf spheroidal galaxy (a companion galaxy of M31) by Da Costa *et al.* (1996) has shown that it too has undergone an extended epoch of star formation. Additionally, evidence was found that suggested that star formation in And I was more centrally concentrated after the initial burst of star formation. The general star formation history of the And I dwarf spheroidal galaxy appears to be similar to that of Leo II (Mighell & Rich 1996). Once the initial global burst of star formation in And I had ended, it appears that the process of star formation never again became efficient enough in the outer regions of that galaxy to allow the formation of large numbers of stars in a secondary global burst of star formation like that observed in the Carina dwarf.

5. SUMMARY

The findings of this paper can be summarized as follows:

- We have determined that the distance modulus of the Carina dwarf spheroidal galaxy is $(m - M)_0 = 19.87 \pm 0.11$ mag. The apparent distance moduli in V and I are $(m - M)_V = 20.05 \pm 0.11$ mag and $(m - M)_I = 19.98 \pm 0.12$ mag, respectively. The reddening of Carina is estimated to be $E(V - I) = 0.08 \pm 0.02$ mag. These determinations assumed that metallicity of the galaxy is $[\text{Fe}/\text{H}] = -1.9 \pm 0.2$ dex.
- The central region of Carina has apparently been forming stars from at least ~ 10.4 Gyr ago to ~ 3.7 Gyr ago; the data is fully consistent with the interpretation of continuous star formation in this region since at least ~ 13 Gyr ago. The median age of the intermediate-age stellar population in the central region of Carina is $\sim 6.5 \pm 0.9$ Gyr. Some stars younger than ~ 3.7 Gyr may well exist in the central region but they are not detected in significant quantities. Little can be determined about the old stellar population due mainly to small field-of-view of the current observation and the large photometric uncertainties observed at the old turnoff magnitudes.
- This space-based observation, when combined with ground-based results, is consistent with the interpretation that the dominant intermediate-age burst of star formation in Carina began in the central region of the galaxy where stars formed for several billion years before the process of star formation became efficient enough in the outer regions of the galaxy to allow for the formation of large numbers of intermediate-age stars.

Our understanding of the star formation history of Carina has been driven by technology. The observations of Mould & Aaronson (1983), Mighell (1990a), and Smecker-Hane *et al.* (1996) used successive generations of CCD camera systems on 4-m class telescopes. The high angular resolution of the the *HST* WFPC2 instrument has provided the next jump in photometric accuracy. Each step along the way, better observations have allowed researchers to study the star formation history of Carina in greater and greater detail. We have studied the star formation history of the central region of the Carina dwarf spheroidal galaxy from the analysis of only 116 stars in a very small field-of-view which surveyed less than 0.5% of Carina. One must be cautious not to over interpret the star formation history of a small fraction of a galaxy as being the global star formation history of that galaxy. Small but significant populations may be missed. For example, Smecker-Hane *et al.* (1996) claim to have detected a 2 Gyr stellar population (~ 3 Gyr on the CDKKS distance scale). We can neither confirm or reject this finding based on the small field-of-view of these WFPC2 observations.

The analysis technique presented in this paper has the potential of being able to produce a detailed description of the the complex global star formation history of Carina with a (theoretical) age resolution much better than 1 Gyr. The present effort was hampered by having only 116 subgiants to study. One can get more stars by surveying more of the galaxy or by obtaining better photometry through longer exposures. A larger and deeper space-based survey would find more subgiants and the longer exposures would enable more stars to be retained at a 99% confidence level due to smaller photometric scatter. Larger and more accurate surveys of Carina will require

the use of state-of-the-art theoretical stellar evolution models. Most of the improvements of the new stellar evolutionary models has occurred in the understanding of stars that are more metal rich than the stellar populations of Carina. The newer isochrones generally produce younger ages for metal-poor globular cluster stars, however the shape of the isochrones of old low-mass Population II stars in the subgiant branch region of the color-magnitude diagram has not changed all that much. The results of this paper are limited by sampling statistics; the RYI models are certainly good enough for the analysis of the the small number of subgiants available in these observations.

The technique outlined in this paper would greatly benefit from the use of stellar evolution models with fine age and metallicity resolutions (e.g. $\Delta t = 0.1$ Gyr and $\Delta[\text{Fe}/\text{H}] = 0.1$ dex, respectively). Such fine age and metallicity resolutions are not currently available with most published theoretical isochrones. If the availability of computation time or hardware constraints are still important limitations, then it would be most helpful if the authors of these theoretical models would also provide accurate interpolation tools. Timing information is very important in the study of star counts in the subgiant branch region. Young stars evolve more quickly through the subgiant branch stage than do older (less massive) stars. This leads to an incompleteness of the counts of younger subgiant branch stars with respect to the older subgiant branch stars. This effect can be rectified if timing information is available from evolutionary tracks. Good observations are also necessary. The derivation of stellar ages from the position of a star within the subgiant branch region of the color-magnitude diagram assumes that the luminosity and effective temperature of the star are not changing rapidly. Once stars evolve through the instability strip (e.g. $\gtrsim 1.5 M_{\odot}$ at near-solar metallicities: Gaitschey & Saio 1996), the proper interpretation of the age of such subgiant branch stars will become problematical. Users of the technique presented in this paper must be sure that the stars they are analyzing have magnitudes that do not vary by more than ~ 0.01 mag.

The analysis of future observations of Carina would benefit from an accurate determination of its reddening and metallicity. This could, for example, be done using the SRM method (Sarajedini 1994) on a shallow but complete survey of red giant branch stars down to about one magnitude below the the horizontal branch ($V \approx 21.7$ mag). Field contamination, especially in the outer regions of the galaxy, can be measured by observing nearby background fields of comparable area and depth. Spectroscopic observations of Carina’s red giants by the Gemini or VLT telescopes will allow researchers to determine the metallicity distribution function of the galaxy. Detailed knowlege about the chemical evolution of the galaxy would provide very useful observational constraints during the determination of a detailed account of Carina’s complex global star formation history.

We would like to thank Taft Armandroff, Ata Sarajedini, Brian Chaboyer, Doug Geisler, Pierre Demarque, Don Vandenberg, Jeff Kuhn, and Gene Byrd for their informative discussions and helpful comments about various aspects of this project. Support for this work was provided by

a grant from the National Aeronautics and Space Administration (NASA), Order No. S-67046-F, which was awarded by the Long-Term Space Astrophysics Program NRA 95-OSS-16. This research has made use of NASA’s Astrophysics Data System Abstract Service and the NASA/IPAC Extragalactic Database (NED) which is operated by the Jet Propulsion Laboratory at Caltech, under contract with the NASA.

A. REVISING THE DISTANCE MODULUS OF CARINA

Smecker-Hane *et al.* (1994) determined the distance modulus of the Carina dwarf spheroidal galaxy to be $(m - M)_0 = 20.12 \pm 0.08$ mag from the mean V magnitude of the horizontal branch, $V_{\text{HB}} = 22.65 \pm 0.05$ mag, and the assumption that the absorption in V is $A_V = 0.08$ mag and that $M_V^{\text{HB}} = M_V^{\text{RR}} = 0.45 \pm 0.07$ mag. The estimate for M_V^{HB} was derived using an assumed metallicity for Carina of $[\text{Fe}/\text{H}] \approx -2.2 \pm 0.4$ dex with the Lee *et al.* (1990, hereafter LDZ) distance scale which gives the absolute V magnitude for RR Lyrae variables as

$$M_{V,\text{LDZ}}^{\text{RR}} = 0.17[\text{Fe}/\text{H}] + 0.82 \quad (\text{A1})$$

for a helium abundance on the main sequence $Y_{\text{MS}} = 0.23$. Based on these assumptions, the V apparent distance modulus of Carina is $(m - M)_V = 20.20 \pm 0.08$ mag.

Lee *et al.* (1993b) have shown that the I magnitude of the tip of the red giant branch (TRGB) of low-mass stars is a good distance indicator for resolved galaxies with old metal-poor ($[\text{Fe}/\text{H}] < -0.7$ dex) stellar populations. Observationally, the absolute I magnitude of the tip of the red giant branch (on the LDZ distance scale) changes little for metallicities less than -0.7 dex : $M_I^{\text{TRGB}} \approx -4.0 \pm 0.1$ mag. Smecker-Hane *et al.* (1994) derived a distance modulus for Carina of $(m - M)_0 = 20.05 \pm 0.09$ mag using the TRGB method (Da Costa & Armandroff 1990, see also Lee *et al.* 1993b) with their measurement of the apparent I magnitude of the tip of the red giant branch, $I_{\text{TRGB}} = 16.15 \pm 0.05$ mag, and their estimate of the color of the TRGB, $(B - I)_0^{\text{TRGB}} = 2.85 \pm 0.05$ mag. This derivation assumed that the metallicity of Carina is $[\text{Fe}/\text{H}] = -2.0 \pm 0.4$ dex, the absorption in I is $A_I = 0.05$ mag, the reddening $E(B - I)$ is 0.05 mag, and $(B - V)/(V - I) = 0.52 \pm 0.01$ mag for stars on the upper red giant branch. Based on these assumptions, the I apparent distance modulus of Carina is $(m - M)_I = 20.10 \pm 0.09$ mag.

Smecker-Hane *et al.* (1994) derive a distance modulus of $(m - M)_0 = 20.09 \pm 0.06$ mag for Carina from their measurements of V_{HB} and I_{TRGB} . This value is the average between 20.12 ± 0.08 mag and 20.05 ± 0.05 mag and the error of 0.06 mag is presumably derived from the simple propagation of errors which assumes that the two determinations were uncorrelated. The derivation of the V apparent distance modulus is directly based on the LDZ distance scale. The derivation of the I apparent distance modulus is based the TRGB method which in turn is based on the work of Da Costa & Armandroff (1990) who used the LDZ distance scale. Since both methods use the LDZ distance scale, the uncertainty of the zeropoint of the $M_{V,\text{LDZ}}^{\text{RR}}$ relation should not be ignored. The distance modulus of Carina reported by Smecker-Hane *et al.* (1994) must have an error at least as large as our current uncertainty of the error associated with the zeropoint of the M_V^{RR} relation: $M_V^{\text{RR}} = -0.60 \pm 0.08$ mag at $[\text{Fe}/\text{H}] = -1.9$ dex (Chaboyer *et al.* 1996a). If we conservatively add in quadrature the 0.06 mag internal errors with a 0.08 mag zeropoint error, we can derive a reasonable estimate of the uncertainty of the Smecker-Hane *et al.* (1994) distance modulus for Carina : $(m - M)_0 = 20.09 \pm 0.10$ mag. Similarly, the Smecker-Hane *et al.* (1996) distance modulus for Carina should presumably be revised to $(m - M)_0 = 20.12 \pm 0.09$ mag.

Da Costa and Hatzidimitriou determined that the metallicity of the Carina dSph galaxy is $[\text{Fe}/\text{H}] = -1.88 \pm 0.08$ dex based on spectroscopic observations of the Ca II triplet in Carina red giants (Da Costa 1993). Using a metallicity estimate of $[\text{Fe}/\text{H}] = -1.9 \pm 0.2$ dex for Carina with the previous observations of V_{HB} and I_{TRGB} by Smecker-Hane *et al.* (1994), we have determined that the V and I apparent distance moduli of Carina on the LDZ distance scale are, respectively, 20.15 ± 0.08 mag and 20.08 ± 0.09 mag.

Observational evidence suggests that the zeropoint for the LDZ relation [Equation (A1)] is about 0.10 mag too bright at $[\text{Fe}/\text{H}] = -1.9$ dex. Chaboyer *et al.* (1996a,b, hereafter CDKKS) reviewed the literature and they advocate the use of the following relation

$$M_{V,\text{CDKKS}}^{\text{RR}} = \left[\begin{array}{c} 0.20 \\ \pm 0.04 \end{array} \right] [\text{Fe}/\text{H}] + \left[\begin{array}{c} 0.98 \\ \pm 0.08 \end{array} \right] \quad (\text{A2})$$

to determine the absolute V magnitude of RR Lyrae stars. This equation gives $M_{V,\text{CDKKS}}^{\text{RR}} = 0.60 \pm 0.11$ mag for $[\text{Fe}/\text{H}] = -1.9$ dex. The absolute bolometric magnitude of RR Lyraes on the CDKKS distance scale can be derived by subtracting the V bolometric correction for RR Lyraes that was used by LDZ, $BC_V^{\text{RR}} = -0.03[\text{Fe}/\text{H}] + 0.01$, from Equation (A2):

$$M_{\text{bol},\text{CDKKS}}^{\text{RR}} = \left[\begin{array}{c} 0.23 \\ \pm 0.04 \end{array} \right] [\text{Fe}/\text{H}] + \left[\begin{array}{c} 0.97 \\ \pm 0.08 \end{array} \right]. \quad (\text{A3})$$

The V bolometric correction for a RR Lyrae star with $[\text{Fe}/\text{H}] = -1.9$ dex is thus 0.07 mag which implies that the absolute bolometric magnitude of the star is $M_{V,\text{bol},\text{CDKKS}}^{\text{RR}} = 0.53 \pm 0.11$ mag. The difference between the LDZ and the CDKKS distance scales at a metallicity of $[\text{Fe}/\text{H}] = -1.9$ dex is $\Delta M_{\text{CDKKS}}^{\text{LDZ}} \approx 0.10$ mag with M_V^{RR} on the CDKKS distance scale being fainter (larger). Using a metallicity estimate of $[\text{Fe}/\text{H}] = -1.9$ dex for Carina with the previous observations of V_{HB} and I_{TRGB} by Smecker-Hane *et al.* (1994), we have determined that the V and I apparent distance moduli of Carina on the CDKKS distance scale are, respectively, 20.05 ± 0.11 mag and 19.98 ± 0.12 mag.

Mould & Aaronson (1983) used a reddening of $E(B-V) = 0.025 \pm 0.01$ mag which was based on the reddening map of Burstein & Heiles (1982) and Burstein (1983, private communication to Mould & Aaronson). Almost all subsequent studies of Carina have either used this reddening or derived reddenings based on this value. Now that a good estimate of the metallicity of Carina is available, it is possible to directly determine the reddening of Carina from CCD photometry. Sarajedini (1994) analyzed the observed red giant branches of Da Costa & Armandroff (1990) and has determined that the $E(V-I)$ reddening is

$$E(V-I) = (V-I)_g - 0.1034[\text{Fe}/\text{H}] - 1.100 \quad (\text{A4})$$

where $(V-I)_g$ is the the apparent $V-I$ color of the red giant branch at the level of the horizontal branch. We have determined from the present observations that the apparent $V-I$ color of the red giant branch at the level of the old horizontal branch is $(V-I)_g = 0.98 \pm 0.02$ mag. With

an assumed metallicity of $[\text{Fe}/\text{H}] = -1.9$ dex, we find that the $E(V-I)$ reddening of Carina is 0.08 ± 0.02 mag. The $E(B-V)$ reddening is 0.06 ± 0.02 mag assuming that $E(V-I) \approx 1.3 E(B-V)$ [Dean *et al.* 1978]. This determination of $E(B-V)$ is higher than but consistent with (at the $\sim 1.6\sigma$ level) the value used by Mould & Aaronson (1983). The absorption in V is determined to be $A_V = 0.19 \pm 0.06$ mag assuming that $A_V = 3.1 E(B-V)$ [Savage & Mathis 1979]. The absorption in I is determined to be $A_I = 0.11 \pm 0.06$ mag from the relation $A_I = A_V - E(V-I)$ mag.

We calculate the distance modulus of the Carina dwarf spheroidal galaxy to be $(m - M)_0 = 19.87 \pm 0.11$ mag. This distance modulus is on the CDKKS distance scale and its value is the average between our estimates for $(m - M)_V - A_V$ and $(m - M)_I - A_I$. The error estimate includes 0.08 mag internal error and a 0.08 mag zeropoint error for the M_V^{RR} relation. The main difference between this distance modulus and those reported by Smecker-Hane *et al.* (1994, 1996) is the 0.10 change due to the use of the CDKKS distance scale instead of the LDZ distance scale. Our higher absorption values for A_V and A_I account for the remaining difference. Kuhn *et al.* (1996) have recently made CCD observations of Carina’s RR Lyaes and they find $V_{\text{HB}} = 20.71 \pm 0.01$ mag in the central region of the galaxy and $V_{\text{HB}} = 20.76 \pm 0.03$ mag in the outer regions of Carina. These new measurements of the V magnitude of the horizontal branch give distance moduli estimates of 19.92 ± 0.12 mag and 19.97 ± 0.12 mag, respectively, on the CDKKS distance scale assuming our standard values $M_{V,\text{CDKKS}}^{\text{RR}} = 0.60 \pm 0.11$ mag for $[\text{Fe}/\text{H}] = -1.9$ dex with $A_V = 0.19 \pm 0.06$ mag.

REFERENCES

- Armandroff, T. E., & Da Costa, G. S. 1991, *AJ*, 101, 1329
- Beauchamp, D., Hardy, E., Suntzeff, N. B., Zinn, R. 1995, *AJ*, 109, 1628
- Biretta, J. A. *et al.* 1996, *WFPC2 Instrument Handbook*, Version 4.0 (STScI, Baltimore)
- Burstein, D., & Heiles, C. 1982, *AJ*, 87, 1165
- Cannon, R. D., Hawarden, T. G., & Tritton, S. B. 1977, *MNRAS*, 180, 81P
- Chaboyer, B., Demarque, P., Kernan, P. J., & Krauss, L. M. 1996, *Science*, 271, 957 (CDKKS : 1 of 2)
- Chaboyer, B., Demarque, P., & Sarajedini, A. 1996, *ApJ*, 459, 558 (CDKKS : 2 of 2)
- Da Costa, G. S. 1993, in *Proc. of the ESO/OHP Workshop on Dwarf Galaxies*, edited by G. Meylan and P. Prugniel (ESO, Garching), p. 221
- Da Costa, G. S., & Armandroff, T. E., 1990, *AJ*, 100, 163
- Da Costa, G., Armandroff, T. E., Caldwell, N., & Seitzer, P. 1996, *AJ*, 112, 2576
- Dean, J. F., Warren, P. R., & Cousins, A. W. J. 1978, *MNRAS*, 183, 569
- Faber, S. M., & Lin, D. C. 1983, *ApJ*, 266, L17
- Gautschi, A., & Saio, H. 1996, *ARA&A*, 34, 551
- Green, E. M., Demarque, P., & King, C. R. 1987, *The Revised Yale Isochrones and Luminosity Functions* (Yale University Observatory, New Haven) (RYI)
- Holtzman, J. A., Hester, J. J., Casertano, S., Trauger, J. T., Watson, A. J., Ballester, G. E., Burrows, C. J., Clarke, J. T., Crisp, D., Evans, R. W., Gallagher J. S., Griffiths, R. E., Hoessel, J. G., Matthews, L. D., Mould, J. R., Scowen, P. A., Stapelfeldt, K. R., & Westphal, J. A. 1995a, *PASP*, 107, 156
- Holtzman, J. A., Burrows, C. J., Casertano, S. Hester, J. J., Trauger, J. T., Watson, A. M., & Worthey, G. S. 1995b, *PASP*, 107, 1065
- Irwin, J., & Hatzidimitriou, D. 1995, *MNRAS*, 277, 1354
- Krist, J. 1993, in *Astronomical Data Analysis Software and Systems II*, ASP Conf. Ser. Vol. 52, edited by R. J. Hanisch, R. J. V. Brissenden, and J. Barnes (ASP, San Francisco), p. 530
- Krist, J. 1994, *Tiny Tim User's Manual Version 4.0* (1994 July 8)
- Kuhn, J. R., Smith, H. A., & Hawley, S. L. 1996, *ApJ*, 469, L93
- Lee, M. G., Freedman, W. L., Mateo, M., Thompson, I., Roth, M., & Ruiz, M.-T. 1993a, *AJ*, 106, 1420
- Lee, M. G., Freedman, W. L., & Madore, B. F. 1993b, *ApJ*, 417, 553
- Lee, Y.-W., Demarque, P., & Zinn, R. 1990, *ApJ*, 350, 155 (LDZ)
- Lee, Y.-W., Demarque, P., & Zinn, R. 1994, *ApJ*, 423, 248
- Mateo, M., Olszewski, E. W., Pryor, C., Welch, D. L., Fischer, P. 1993, *AJ*, 105, 510
- Mighell, K. J. 1990a, *A&AS*, 82, 1
- Mighell, K. J. 1990b, Ph.D. thesis, University of Groningen
- Mighell, K. J. 1990c, *A&AS*, 82, 207
- Mighell, K. J., & Butcher, H. R. 1992, *A&A*, 255, 26
- Mighell, K. J., & Rich, R. M. 1995, *AJ*, 110, 1649
- Mighell, K. J., & Rich, R. M. 1996, *AJ*, 111, 777
- Mighell, K. J., Rich, R. M., Shara, M., & Fall, M. 1996, *AJ*, 111, 2314
- Mould, J. R., & Aaronson, M. 1983, *ApJ*, 273, 530
- Saha, A., Monet, D.G., & Seitzer, P. 1986, *AJ*, 92, 302
- Sarajedini, A. 1994, *AJ*, 107, 618
- Sarajedini, A., Lee, Y.-W., & Lee, D.-H. 1995, *ApJ*, 450, 712
- Savage, B. D., & Mathis, J. S. 1979, *ARA&A*, 17, 73
- Smecker-Hane, T., Stetson, P. B., Hesser, J. E., & Lehnert, M. D. 1994, *AJ*, 108, 507

- Smecker-Hane, T. A., Stetson, P. B., Hesser, J. E. & VandenBerg, D. A. 1996, in *From Stars to Galaxies: The Impact of Stellar Physics on Galaxy Evolution*, ASP Conf. Ser. Vol. 98, edited by C. Leitherer, U. Fritze-von Alvensleben, and J. Huchra (ASP, San Francisco), p. 328
- Smecker-Hane, T. A. 1997, in *Star Formation, Near and Far*, AIP Conf. Proc. No. 393, edited by S. Holt & L. G. Mundy (AIP, New York), p. 571
- Vogt, S., Mateo, M., Olszewski, E. W., & Keane, M. J. 1995, *AJ*, 109, 151

Fig. 1.— The V vs $V-I$ color-magnitude diagram and apparent V stellar luminosity function of the observed stellar field in the Carina dwarf spheroidal galaxy. The error bars in the color-magnitude diagram indicate r.m.s. (1σ) uncertainties for a single star at the corresponding magnitude. The error bars for the apparent V stellar luminosity function are derived from counting (Poisson) statistics. This figure shows 2025 stars down to $V = 26.0$ mag and 3,185 stars down to a limiting magnitude of $V \approx 27.2$ mag on the main sequence of Carina. The *Hubble Space Telescope* WFPC2 instrument was used to make two 2200 s observations with the F555W and F814W filters.

Fig. 2.— The apparent V stellar luminosity function of the Carina WFPC2 field is shown (filled circles) with the Carina stellar luminosity function (open diamonds) of Mighell (1990c) which has been scaled down by a factor of 3.2. The open diamonds are plotted 0.04 mag too faint to improve readability. For comparison, the 6, 8, and 14 Gyr theoretical RYI (Green *et al.* 1987) stellar luminosity functions for metallicity $Z = 0.00025$ ($[\text{Fe}/\text{H}] = -1.9$) and helium abundance $Y = 0.24$ are respectively displayed as the solid, dashed, and dotted curves. The RYI stellar luminosity functions are plotted using an apparent V distance modulus of $(m - M)_V = 20.05$ mag and have been normalized to have the same number of stars as the apparent Carina stellar luminosity function in the magnitude range $25.0 \leq V \leq 26.0$. See the text for further details.

Fig. 3.— The V vs $V-I$ color-magnitude diagram of the main-sequence turnoff region of the Carina dwarf spheroidal galaxy. The error bars indicate 1σ uncertainties for a single star at the corresponding magnitude. The theoretical RYI isochrones for ages 2 to 18 Gyr (left to right) are displayed with 2 Gyr steps for $Z = 0.00025$ ($[\text{Fe}/\text{H}] = -1.9$) and $Y = 0.24$. The isochrones have been displayed using an apparent V distance modulus $(m - M)_V = 20.05$ mag and a reddening $E(V-I) = 0.08$ mag.

Fig. 4.— The V vs $V-I$ color-magnitude diagram of the main-sequence turnoff region of the Carina dwarf spheroidal galaxy. The error bars indicate 1σ uncertainties for a single star at the corresponding magnitude. The theoretical RYI isochrones for ages 2 to 18 Gyr (left to right, bottom to top) are displayed with 1 Gyr steps for $Z = 0.00025$ and $Y = 0.24$. The isochrones have been displayed using an apparent V distance modulus $(m - M)_V = 20.05$ mag and a reddening $E(V-I) = 0.08$ mag. The interpolated isochrones have also been plotted (at 0.25 Gyr increments) from a point on the isochrone near the main-sequence turnoff (long-dashed curve) to the base of the red giant branch [short-dashed line at $(V-I)_0 = 0.70$ mag]. See the text for further details.

Fig. 5.— This figure shows the 1000 simulated observations (dots) for all of the 152 stars (asterisks) found in the bounded region of Fig. 4. The scatter of the simulated observations for an individual star appears to be elliptical principally due to the standard 5:1 plotting ratio of the magnitude scales ($V:V-I$) used in the figure. A total of 92.7% of the simulated observations were found within the bounded region. The other details of the figure are described in Fig. 4. See the text for further details.

Fig. 6.— The r.m.s. errors of the stellar age estimates increase with age because photometric

errors increase with apparent magnitude and the spacing between theoretical isochrones generally decrease with increasing age. This figure shows the distribution of estimated ages for the 1000 simulated observations of the stars 246342968 (dashed histogram), 409901113 (dotted histogram), and 269902650 (solid histogram), which have an estimated stellar ages of 5.04 ± 0.25 , 6.87 ± 0.35 , and 9.70 ± 0.52 Gyr, respectively. The figure shows that the simulated observations of these stars were spread, respectively, over 2, 6, and 10 bins that are 0.25 Gyr wide.

Fig. 7.— The mean estimated ages (in Gyr on the RYI age scale) and r.m.s. errors of all 152 stars in the bounded region of Fig. 4. Table 3 is the source of the data. There are 116 stars (filled squares) that had at least 897 of the 1000 simulated observations found within the bounded region of Fig. 4 ($p \geq 0.897$). The 36 remaining stars are shown as open squares. See the text for further details.

Fig. 8.— This figure shows the 1000 simulated observations (dots) for the 116 stars (asterisks) found in the bounded region of Fig. 4 with at least a 99% probability of actually being found within the bounded region. The remaining 36 stars (squares) out of the original 152 found bounded region are also shown. The other details of the figure are as described in Fig. 5. See the text for further details.

Fig. 9.— The estimated mean stellar ages (in Gyr on the RYI age scale) of the conservative subset of 116 subgiant branch stars ($p \geq 0.897 \Rightarrow p' \geq 0.990$). The errors for all these stars are shown as filled squares in Fig. 7. Two 0.25 Gyr wide bins were added together to produce 2 low-resolution star-count histograms with 0.5 Gyr bin widths that are offset by one bin from each other: the vertical-shaded histogram gives the counts at 2.00, 2.50, 3.00, 3.50, ... Gyr; the horizontal-shaded histogram gives the counts at 2.25, 2.75, 3.25, 3.75, ... Gyr. See the text for further details.

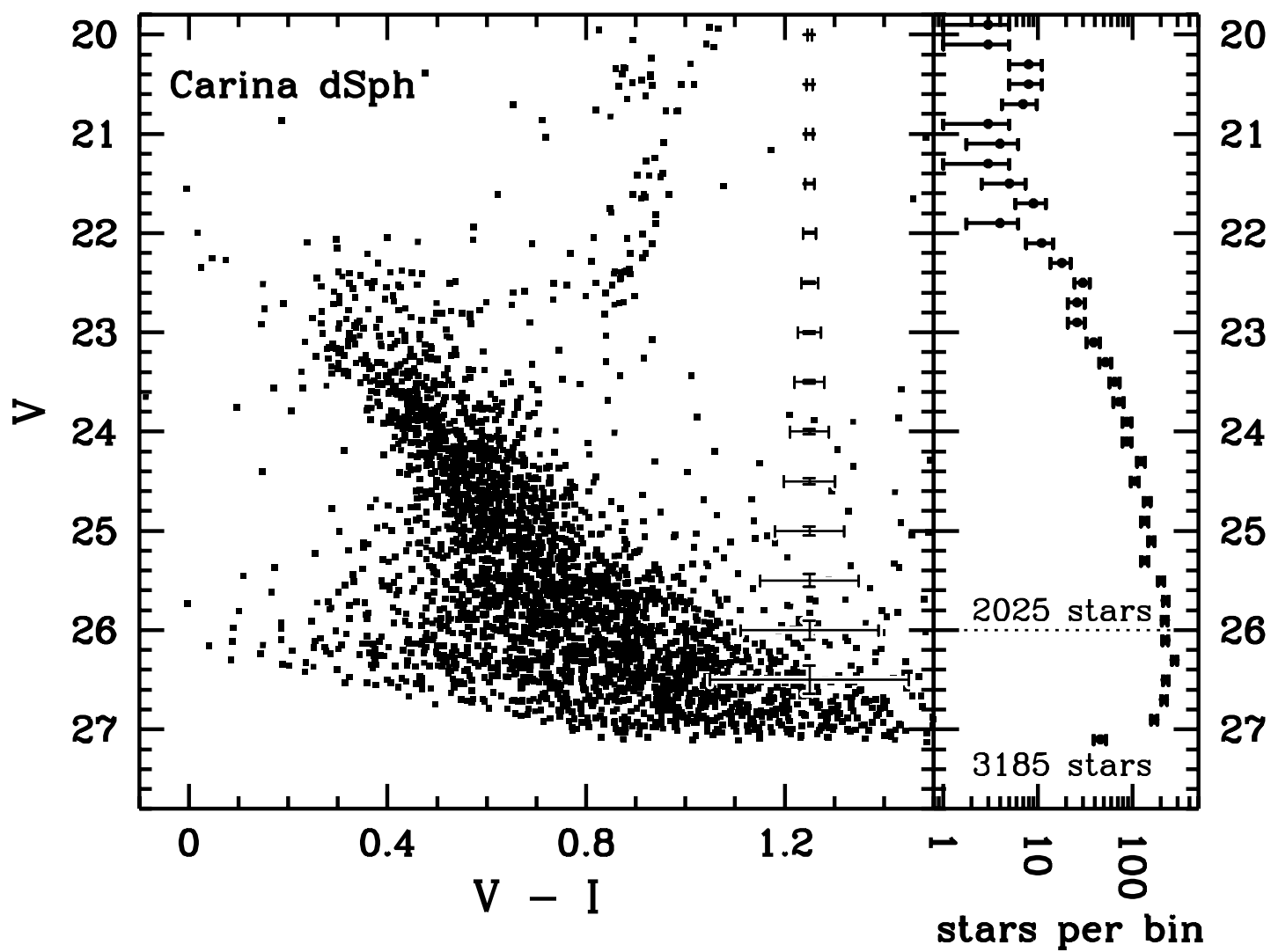


Figure 1 of Mighell (1997)

TABLE 1. Aperture corrections.

Filter	CCD	r [pix]	$\langle\Delta_r\rangle$ [mag]	δ_r [mag]
F555W	WF2	1.8	-0.211 \pm 0.011	0.003 \pm 0.005
F555W	WF3	1.8	-0.275 \pm 0.020	0.023 \pm 0.005
F555W	WF4	1.8	-0.232 \pm 0.009	0.005 \pm 0.005
F814W	WF2	1.8	-0.240 \pm 0.012	-0.026 \pm 0.005
F814W	WF3	1.8	-0.300 \pm 0.019	-0.013 \pm 0.005
F814W	WF4	1.8	-0.259 \pm 0.009	-0.021 \pm 0.005

Table 1 of Mighell (1997)

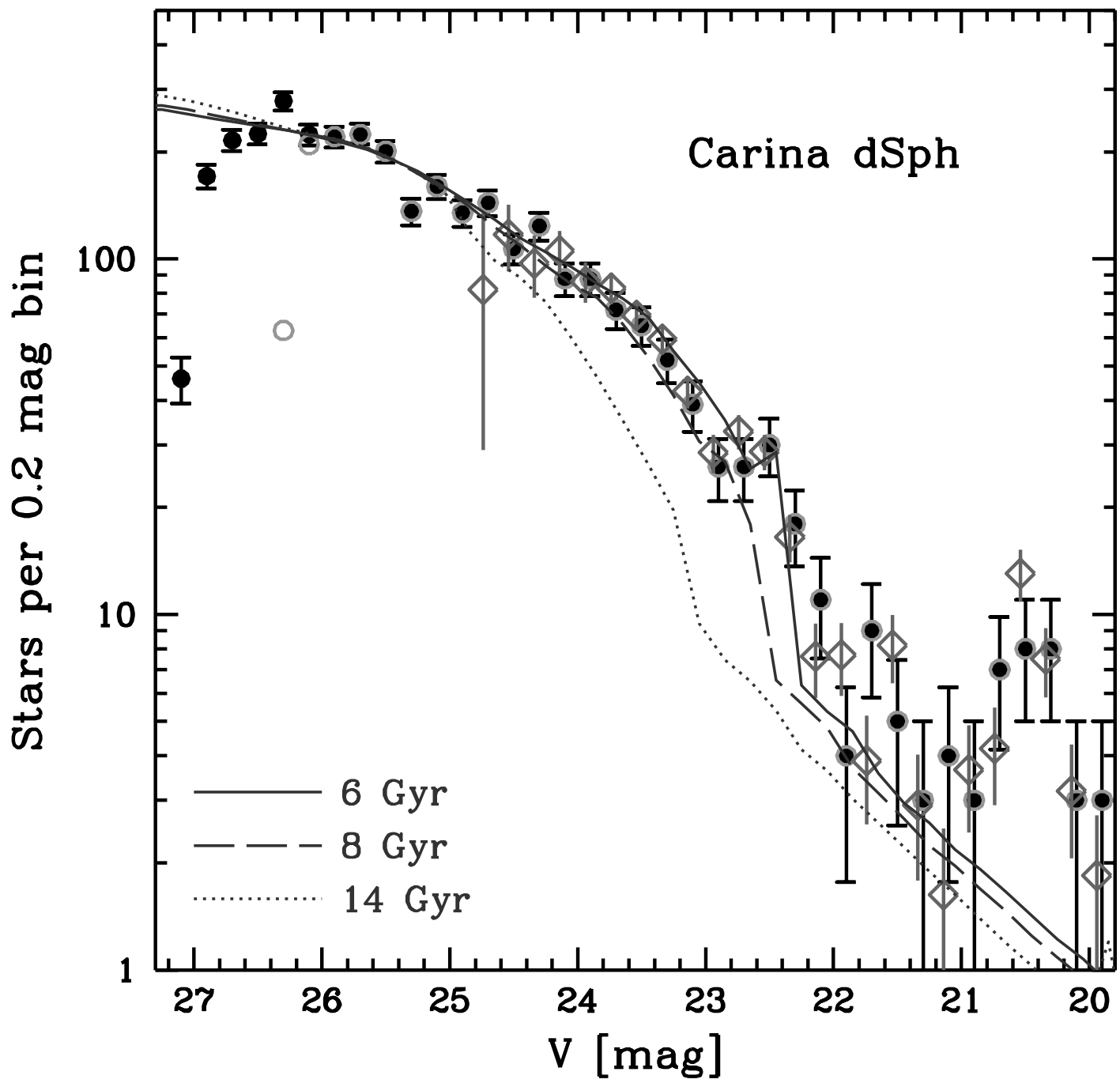


Figure 2 of Mighell (1997)

TABLE 2. WFPC2 stellar photometry in the Carina dSph galaxy

ID	V [mag]	σ_V [mag]	$V - I$ [mag]	$\sigma_{(V-I)}$ [mag]
206092291	26.451	0.135	1.016	0.181
206096331	25.933	0.085	0.745	0.128
206196888	24.177	0.026	0.539	0.041
206281059	25.114	0.046	0.761	0.069
206320926	24.226	0.025	0.652	0.040
206322440	26.451	0.128	1.186	0.164
206354893	23.811	0.020	0.481	0.033
206357260	25.362	0.055	0.853	0.081
206502142	24.571	0.032	0.514	0.053
206583310	26.977	0.204	1.942	0.221
206711900	25.897	0.081	0.567	0.132
206723435	25.144	0.047	0.551	0.076
206754663	23.851	0.021	0.435	0.035
206775798	25.210	0.050	0.539	0.082
206864990	25.710	0.072	0.862	0.102
206982045	23.165	0.015	0.446	0.024
207021398	26.719	0.163	1.399	0.195
207086846	26.259	0.112	0.910	0.158
207184577	24.348	0.028	0.443	0.047
207205832	26.431	0.129	1.238	0.163

Table 2 of Mighell (1997)

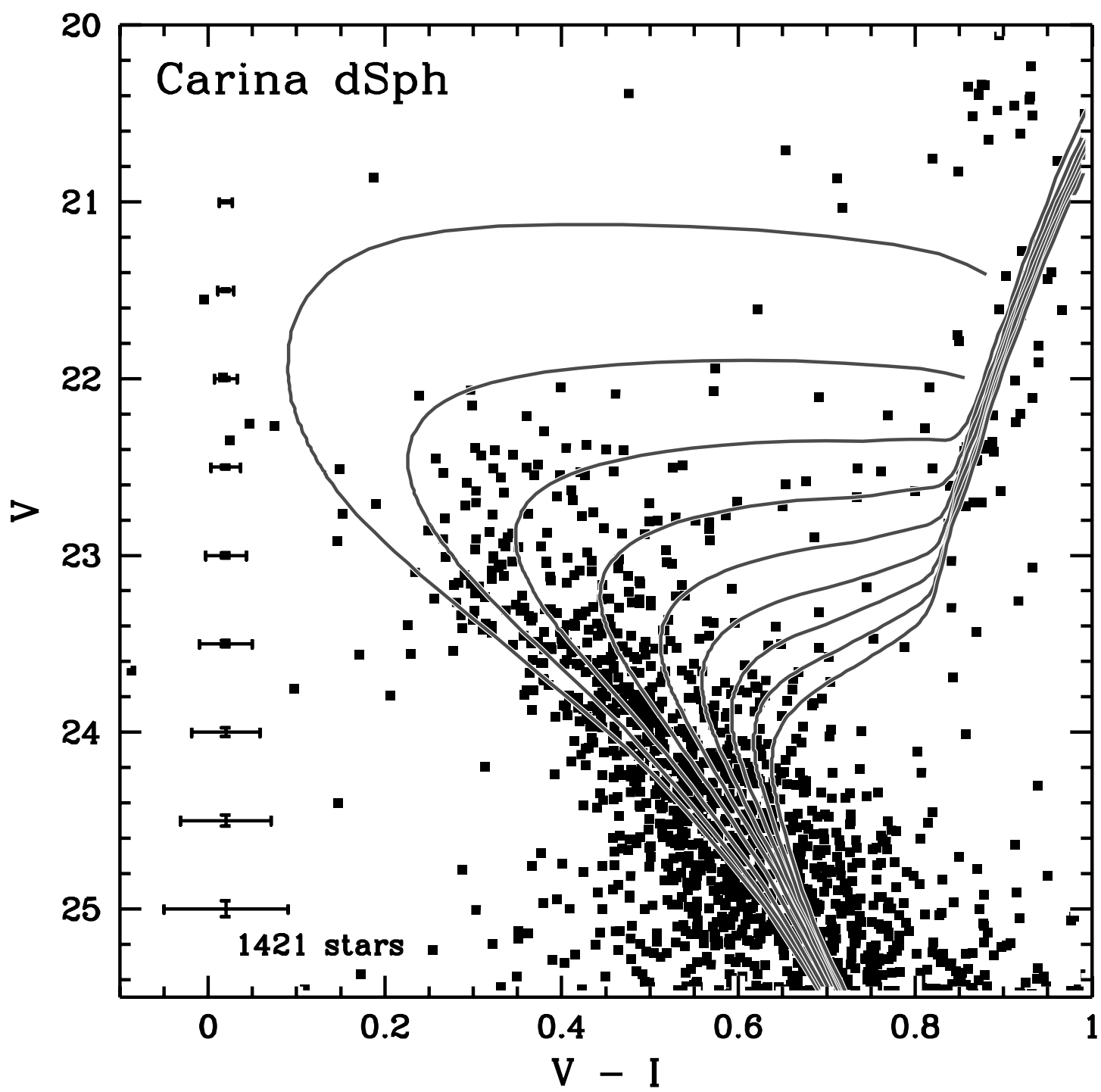


Figure 3 of Mighell (1997)

Table 3. Stellar photometry and statistics of selected stars in Carina

ID	V	σ_V	V-I	$\sigma_{(V-I)}$	p	t'_{Gyr}	$\langle t_{\text{Gyr}} \rangle$	$\sigma_{(t_{\text{Gyr}})}$	ID	V	σ_V	V-I	$\sigma_{(V-I)}$	p	t'_{Gyr}	$\langle t_{\text{Gyr}} \rangle$	$\sigma_{(t_{\text{Gyr}})}$
206982045	23.165	0.015	0.446	0.024	0.983	8.13	8.09	0.62	357274003	22.374	0.009	0.428	0.016	1.000	5.63	5.53	0.25
208776728	23.265	0.017	0.480	0.026	0.984	8.88	8.93	0.70	358912958	22.868	0.013	0.318	0.022	0.750	5.38	5.62	0.44
209716363	22.705	0.012	0.499	0.019	1.000	7.38	7.26	0.29	362217251	23.523	0.019	0.530	0.030	0.794	10.63	11.00	0.92
210786207	22.582	0.011	0.676	0.016	1.000	7.38	7.35	0.22	362233206	22.558	0.012	0.331	0.019	1.000	5.38	5.40	0.34
211067035	22.698	0.011	0.599	0.018	1.000	7.88	7.80	0.26	365657590	22.721	0.011	0.650	0.018	1.000	8.13	8.15	0.25
216834267	22.634	0.011	0.411	0.018	1.000	6.38	6.34	0.30	367234740	23.379	0.017	0.572	0.027	1.000	11.38	11.43	0.77
217205332	23.427	0.017	0.515	0.027	0.912	10.13	10.22	0.80	368833706	22.784	0.012	0.529	0.019	1.000	7.88	7.85	0.29
217471191	22.896	0.012	0.339	0.021	0.906	5.88	5.91	0.48	369800850	22.879	0.013	0.344	0.022	0.945	5.88	5.94	0.50
218040930	23.658	0.019	0.668	0.029	0.967	16.13	16.02	1.04	374075022	23.015	0.015	0.407	0.024	0.993	7.13	7.15	0.56
218152172	23.144	0.014	0.488	0.023	1.000	8.88	8.84	0.55	375067507	23.261	0.015	0.488	0.026	0.986	9.13	9.09	0.71
218274642	22.811	0.012	0.567	0.019	1.000	8.38	8.24	0.30	375927735	23.750	0.020	0.622	0.033	0.944	15.13	15.22	1.41
219227798	23.379	0.017	0.596	0.026	1.000	11.88	11.94	0.74	376423239	22.545	0.012	0.398	0.019	1.000	5.88	5.92	0.29
221263072	22.955	0.013	0.351	0.022	0.843	6.13	6.17	0.49	376881815	22.917	0.014	0.568	0.021	1.000	8.88	8.85	0.34
222232441	22.872	0.012	0.384	0.020	1.000	6.63	6.60	0.44	406654698	22.490	0.009	0.537	0.016	1.000	6.38	6.44	0.24
223493561	22.534	0.012	0.266	0.019	1.000	4.63	4.57	0.40	408640863	22.097	0.009	0.239	0.015	1.000	3.88	3.76	0.26
223867553	23.674	0.019	0.616	0.030	0.988	14.38	14.43	1.28	409901113	22.778	0.012	0.423	0.020	1.000	6.88	6.87	0.35
225033399	23.035	0.014	0.383	0.023	0.897	6.63	6.75	0.54	409911253	22.208	0.008	0.769	0.013	0.773	5.38	5.29	0.25
226556928	24.068	0.025	0.634	0.038	0.138	17.63	17.25	0.60	410076638	23.243	0.017	0.454	0.026	0.891	8.38	8.37	0.66
227607411	23.427	0.017	0.516	0.027	0.898	10.13	10.20	0.79	410744287	23.020	0.014	0.465	0.023	1.000	8.13	8.10	0.48
227622966	23.270	0.015	0.488	0.024	0.992	9.13	9.09	0.68	410972897	22.597	0.011	0.653	0.017	1.000	7.38	7.38	0.21
227915261	22.808	0.012	0.499	0.019	1.000	7.63	7.72	0.31	413152269	23.525	0.018	0.691	0.027	0.993	15.38	15.35	0.87
228996404	23.791	0.022	0.630	0.034	0.893	15.88	15.59	1.39	413254247	23.531	0.018	0.515	0.029	0.620	10.13	10.82	0.82
230502334	23.074	0.014	0.464	0.023	0.999	8.13	8.22	0.52	414534472	22.065	0.007	0.297	0.014	1.000	4.13	4.02	0.25
230794232	23.245	0.015	0.447	0.025	0.847	8.13	8.26	0.63	415315531	22.545	0.011	0.426	0.018	1.000	6.13	6.13	0.27
232495291	23.402	0.016	0.642	0.025	1.000	13.13	13.08	0.63	415520642	22.392	0.009	0.405	0.016	1.000	5.38	5.48	0.25
234326920	22.106	0.008	0.691	0.013	1.000	4.88	4.87	0.17	416044092	22.505	0.011	0.360	0.018	1.000	5.63	5.54	0.29
239597344	22.430	0.010	0.345	0.017	1.000	5.13	5.21	0.29	418784989	22.644	0.012	0.335	0.019	1.000	5.63	5.59	0.37
244922515	23.371	0.017	0.564	0.026	1.000	11.13	11.19	0.77	419987515	22.487	0.011	0.373	0.018	1.000	5.63	5.59	0.28
245707411	23.832	0.022	0.624	0.033	0.827	15.88	15.74	1.33	421161945	22.504	0.011	0.526	0.017	1.000	6.38	6.47	0.25
246342968	22.298	0.009	0.380	0.015	1.000	5.13	5.04	0.25	422020900	23.191	0.014	0.593	0.023	1.000	10.63	10.73	0.49
248021667	23.225	0.015	0.539	0.024	1.000	10.13	10.00	0.59	424401693	23.982	0.024	0.624	0.037	0.393	16.38	16.76	0.92
248713670	23.719	0.020	0.585	0.031	0.813	13.38	13.73	1.25	424847378	22.048	0.009	0.399	0.014	1.000	4.38	4.36	0.19
250433446	23.260	0.015	0.501	0.024	0.998	9.38	9.36	0.69	426000628	22.087	0.009	0.461	0.014	1.000	4.63	4.63	0.16
252891810	22.803	0.012	0.509	0.019	1.000	7.88	7.78	0.31	431367216	22.950	0.015	0.336	0.024	0.667	5.63	6.01	0.45
253255994	23.483	0.017	0.523	0.028	0.845	10.38	10.63	0.84	432071274	23.040	0.014	0.519	0.022	1.000	8.88	8.93	0.43
254302341	22.950	0.013	0.377	0.022	0.987	6.63	6.56	0.52	432965766	23.183	0.015	0.745	0.023	0.930	12.63	12.70	0.55
254953594	22.453	0.010	0.257	0.017	1.000	4.38	4.42	0.35	433237892	23.455	0.017	0.567	0.028	0.997	11.63	11.59	0.90
256051426	21.607	0.008	0.622	0.011	1.000	3.13	3.13	0.13	433552487	22.802	0.012	0.551	0.019	1.000	8.13	8.09	0.29
257336181	23.049	0.014	0.525	0.022	1.000	9.13	9.05	0.43	434337862	22.880	0.014	0.494	0.021	1.000	7.88	7.97	0.37
258487633	22.846	0.014	0.448	0.021	1.000	7.38	7.36	0.39	435421295	22.407	0.009	0.470	0.016	1.000	5.88	5.83	0.23
260553627	22.701	0.012	0.303	0.020	0.996	5.13	5.20	0.46	435764561	23.612	0.019	0.550	0.030	0.735	11.63	12.04	1.00
261711981	22.688	0.012	0.413	0.019	1.000	6.63	6.51	0.32	436436102	22.403	0.010	0.324	0.017	1.000	4.88	4.98	0.29
262465749	22.068	0.008	0.572	0.013	1.000	4.63	4.63	0.14	438604368	22.982	0.014	0.429	0.023	1.000	7.38	7.48	0.49
265413332	22.851	0.013	0.567	0.020	1.000	8.38	8.48	0.31	438786939	23.141	0.015	0.388	0.025	0.512	6.63	7.16	0.49
265606146	22.666	0.012	0.395	0.019	1.000	6.38	6.27	0.33	440142268	22.671	0.012	0.734	0.018	0.992	8.13	8.04	0.27
265873880	23.154	0.015	0.406	0.024	0.734	7.13	7.38	0.52	440431604	22.437	0.010	0.309	0.017	1.000	4.88	4.94	0.30
269902650	23.165	0.014	0.536	0.023	1.000	9.63	9.70	0.52	442611990	23.769	0.020	0.576	0.033	0.612	12.88	13.95	1.14
271282630	22.971	0.012	0.518	0.021	1.000	8.63	8.63	0.38	442662747	23.029	0.014	0.434	0.023	1.000	7.63	7.62	0.53
273011135	23.230	0.015	0.529	0.024	1.000	9.88	9.87	0.60	444464559	23.707	0.020	0.631	0.031	0.982	15.13	15.15	1.30
273882750	23.823	0.022	0.655	0.033	0.699	17.13	16.43	1.17	446185586	23.364	0.017	0.521	0.028	0.985	10.13	10.13	0.83
275783663	22.755	0.012	0.436	0.019	1.000	6.88	6.93	0.33	448397605	23.575	0.019	0.702	0.029	0.944	16.13	16.12	0.96
278524200	23.249	0.017	0.445	0.026	0.785	8.13	8.24	0.61	451083858	22.773	0.012	0.586	0.019	1.000	8.13	8.17	0.29
310300992	23.910	0.022	0.649	0.034	0.520	17.63	16.51	1.11	451792052	22.547	0.012	0.369	0.019	1.000	5.63	5.71	0.31
313671760	23.762	0.022	0.601	0.033	0.846	14.13	14.66	1.36	453943099	22.590	0.010	0.293	0.019	1.000	4.88	4.99	0.39
313972676	23.621	0.019	0.607	0.030	0.995	13.88	13.76	1.19	456166637	23.161	0.017	0.489	0.028	0.999	8.88	8.86	0.65
314671663	22.635	0.010	0.303	0.019	1.000	5.13	5.16	0.42	457692999	22.210	0.009	0.360	0.016	1.000	4.63	4.69	0.24
315284928	22.766	0.012	0.362	0.021	1.000	6.13	6.11	0.43	458107399	23.321	0.016	0.691	0.025	1.000	13.13	13.22	0.60
317853886	22.896	0.013	0.686	0.020	1.000	9.63	9.54	0.29	458750671	22.929	0.013	0.334	0.022	0.723	5.63	5.92	0.47
319457656	22.771	0.012	0.322	0.021	0.990	5.63	5.51	0.48	461155388	23.872	0.022	0.599	0.035	0.571	14.38	15.58	1.26
320234698	22.876	0.014	0.468	0.021	1.000	7.63	7.68	0.37	461313441	23.654	0.020	0.559	0.031	0.733	11.88	12.60	1.11
321052944	22.150	0.009	0.299	0.015	1.000	4.13	4.24	0.26	462227388	23.472	0.018	0.753	0.027	0.844	16.63	16.38	0.95
3211190629	23.122	0.013	0.387	0.024	0.610	6.63	7.05	0.48	463392405	23.511	0.019	0.634	0.029	1.000	13.88	13.78	0.89
321427567	21.941	0.008	0.574	0.013	1.000	4.13	4.13	0.15	464606720	22.524	0.011	0.761	0.016	0.853	7.13	7.09	0.24
321605219	23.205	0.015	0.476	0.025	0.996	8.63	8.72	0.65	465594919	23.297	0.0						

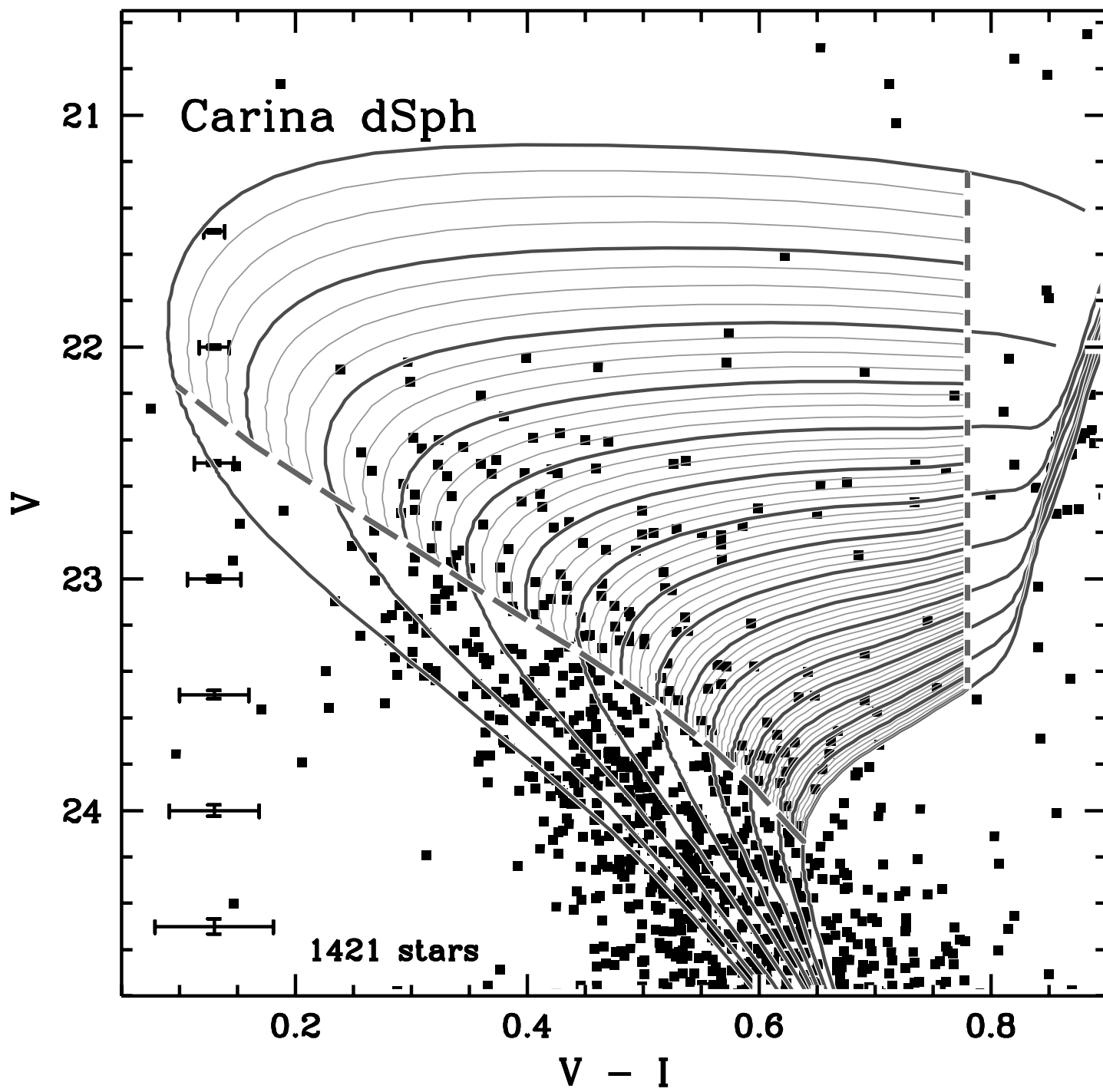


Figure 4 of Mighell (1997)

Table 4. Summary of the recovery probabilities of Table 3.

i	p	n_i	$\sum n_i$	\sum in	\sum out	p'	ID
0	1.000	77	77	77000	0	1.000	
1	0.999	3	80	79997	3	1.000	
2	0.998	3	83	82991	9	1.000	
3	0.997	2	85	84985	15	1.000	
4	0.996	2	87	86977	23	1.000	
5	0.995	1	88	87972	28	1.000	313972676
7	0.993	2	90	89958	42	1.000	
8	0.992	3	93	92934	66	0.999	
10	0.990	1	94	93924	76	0.999	319457656
12	0.988	2	96	95900	100	0.999	
13	0.987	1	97	96887	113	0.999	254302341
14	0.986	1	98	97873	127	0.999	375067507
15	0.985	1	99	98858	142	0.999	446185586
16	0.984	1	100	99842	158	0.998	208776728
17	0.983	1	101	100825	175	0.998	206982045
18	0.982	1	102	101807	193	0.998	444464559
21	0.979	1	103	102786	214	0.998	328073648
33	0.967	1	104	103753	247	0.998	218040930
38	0.962	1	105	104715	285	0.997	335956718
46	0.954	1	106	105669	331	0.997	343027840
55	0.945	1	107	106614	386	0.996	369800850
56	0.944	2	109	108502	498	0.995	
70	0.930	1	110	109432	568	0.995	432965766
75	0.925	2	112	111282	718	0.994	
88	0.912	1	113	112194	806	0.993	217205332
94	0.906	1	114	113100	900	0.992	217471191
102	0.898	1	115	113998	1002	0.991	227607411
103	0.897	1	116	114895	1105	0.990	225033399
107	0.893	1	117	115788	1212	0.990	228996404
109	0.891	1	118	116679	1321	0.989	410076638
123	0.877	1	119	117556	1444	0.988	344864108
126	0.874	1	120	118430	1570	0.987	467424588
129	0.871	1	121	119301	1699	0.986	341227307
147	0.853	1	122	120154	1846	0.985	464606720
153	0.847	1	123	121001	1999	0.984	230794232
154	0.846	1	124	121847	2153	0.983	313671760
155	0.845	1	125	122692	2308	0.982	253255994
156	0.844	1	126	123536	2464	0.980	462227388
157	0.843	1	127	124379	2621	0.979	221263072
172	0.828	1	128	125207	2793	0.978	465594919
173	0.827	1	129	126034	2966	0.977	245707411
187	0.813	1	130	126847	3153	0.976	248713670
206	0.794	1	131	127641	3359	0.974	362217251
215	0.785	1	132	128426	3574	0.973	278524200
219	0.781	1	133	129207	3793	0.971	465633103
227	0.773	1	134	129980	4020	0.970	409911253
250	0.750	1	135	130730	4270	0.968	358912958
265	0.735	1	136	131465	4535	0.967	435764561
266	0.734	1	137	132199	4801	0.965	265873880
267	0.733	1	138	132932	5068	0.963	461313441
271	0.729	1	139	133661	5339	0.962	325294154
277	0.723	1	140	134384	5616	0.960	458750671
301	0.699	1	141	135083	5917	0.958	273882750
333	0.667	1	142	135750	6250	0.956	431367216
338	0.662	1	143	136412	6588	0.954	347535325
380	0.620	1	144	137032	6968	0.952	413254247
388	0.612	1	145	137644	7356	0.949	442611990
390	0.610	1	146	138254	7746	0.947	321190629
429	0.571	1	147	138825	8175	0.944	461155388
480	0.520	1	148	139345	8655	0.942	310300992
488	0.512	1	149	139857	9143	0.939	438786939
492	0.508	1	150	140365	9635	0.936	469023344
607	0.393	1	151	140758	10242	0.932	424401693
862	0.138	1	152	140896	11104	0.927	226556928

Table 4 of Mighell (1997)

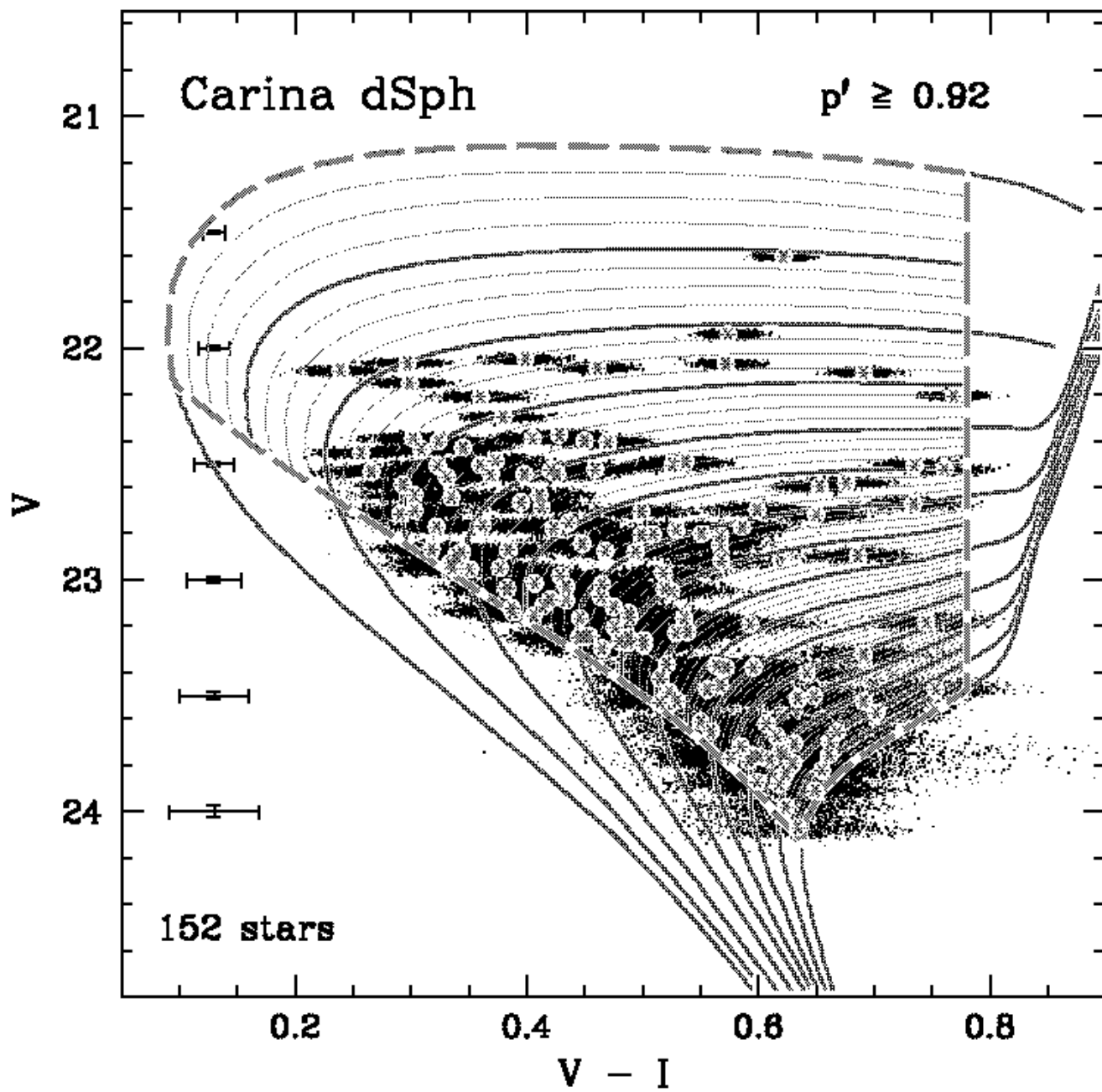


Figure 5 of Mighell (1997) --- low resolution

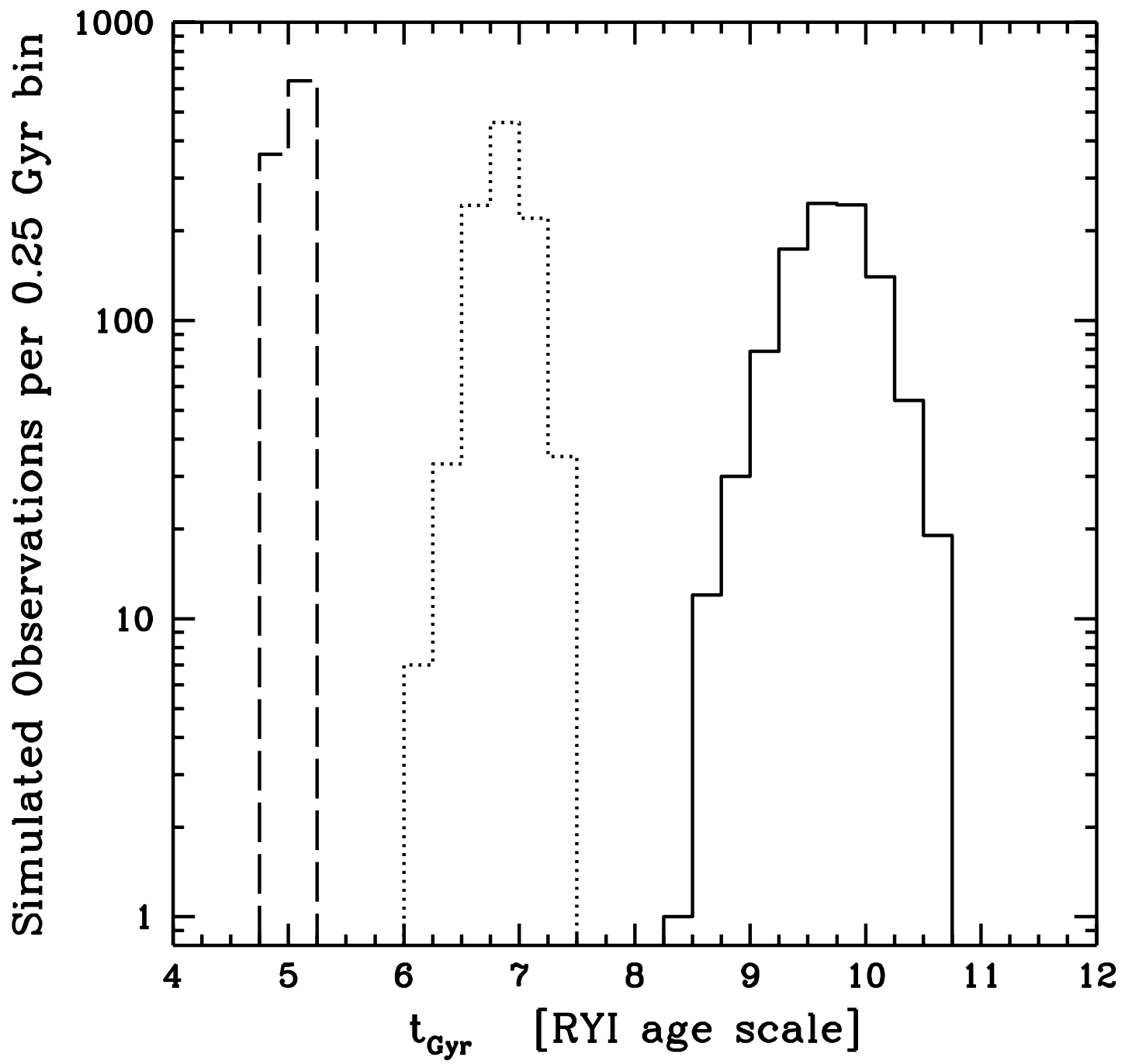


Figure 6 of Mighell (1997)

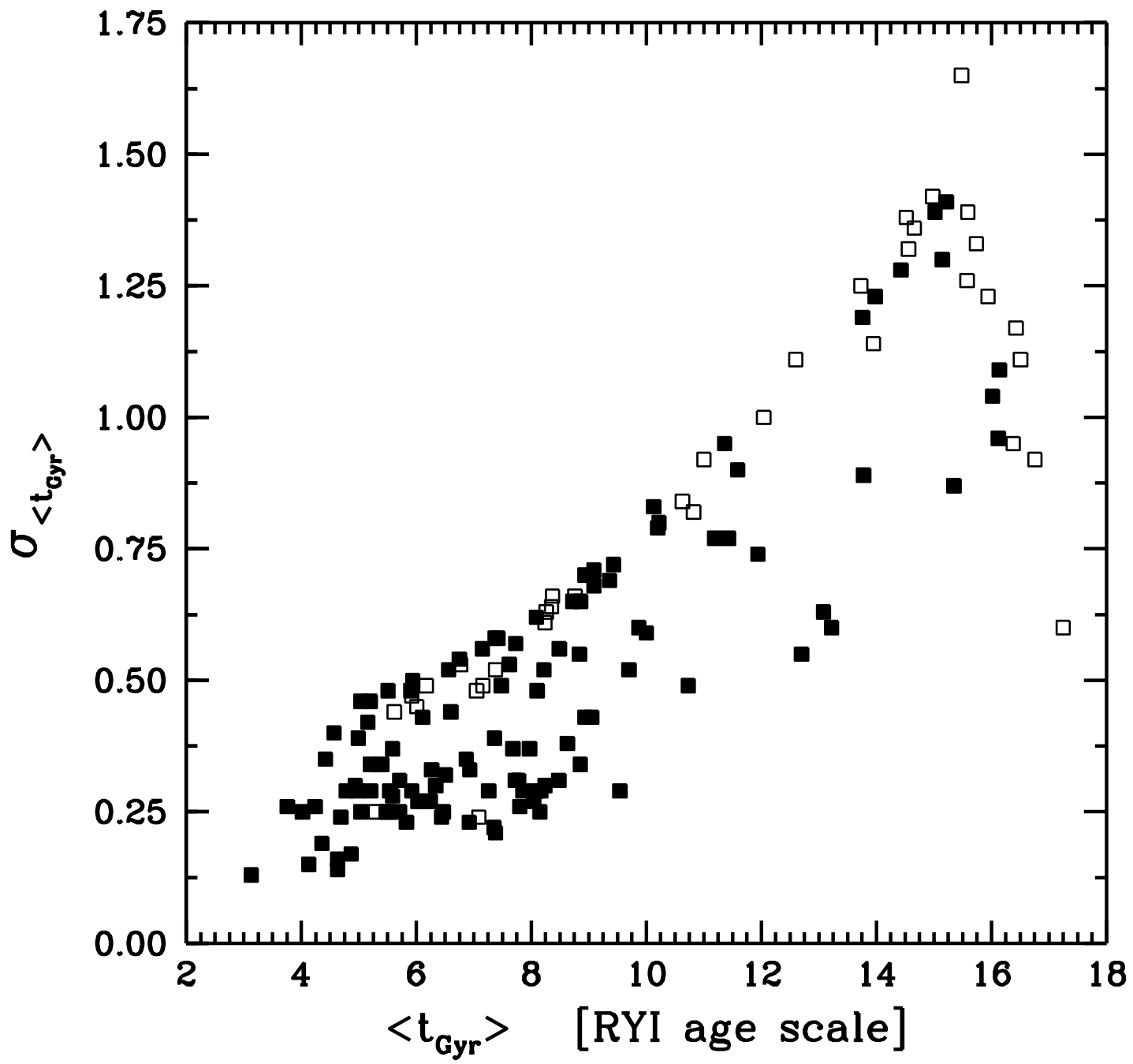


Figure 7 of Mighell (1997)

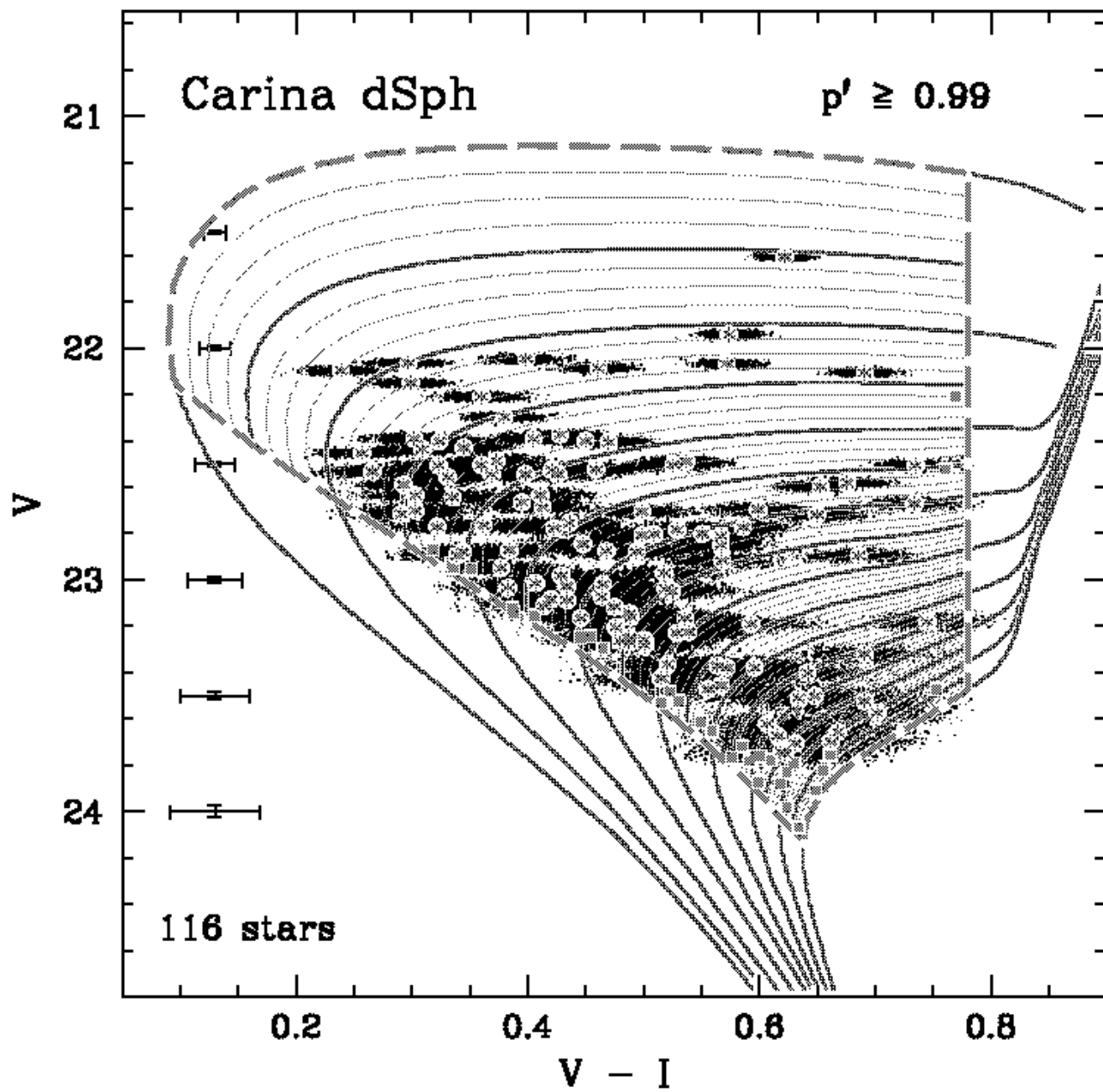


Figure 8 of Mighell (1997) --- low resolution

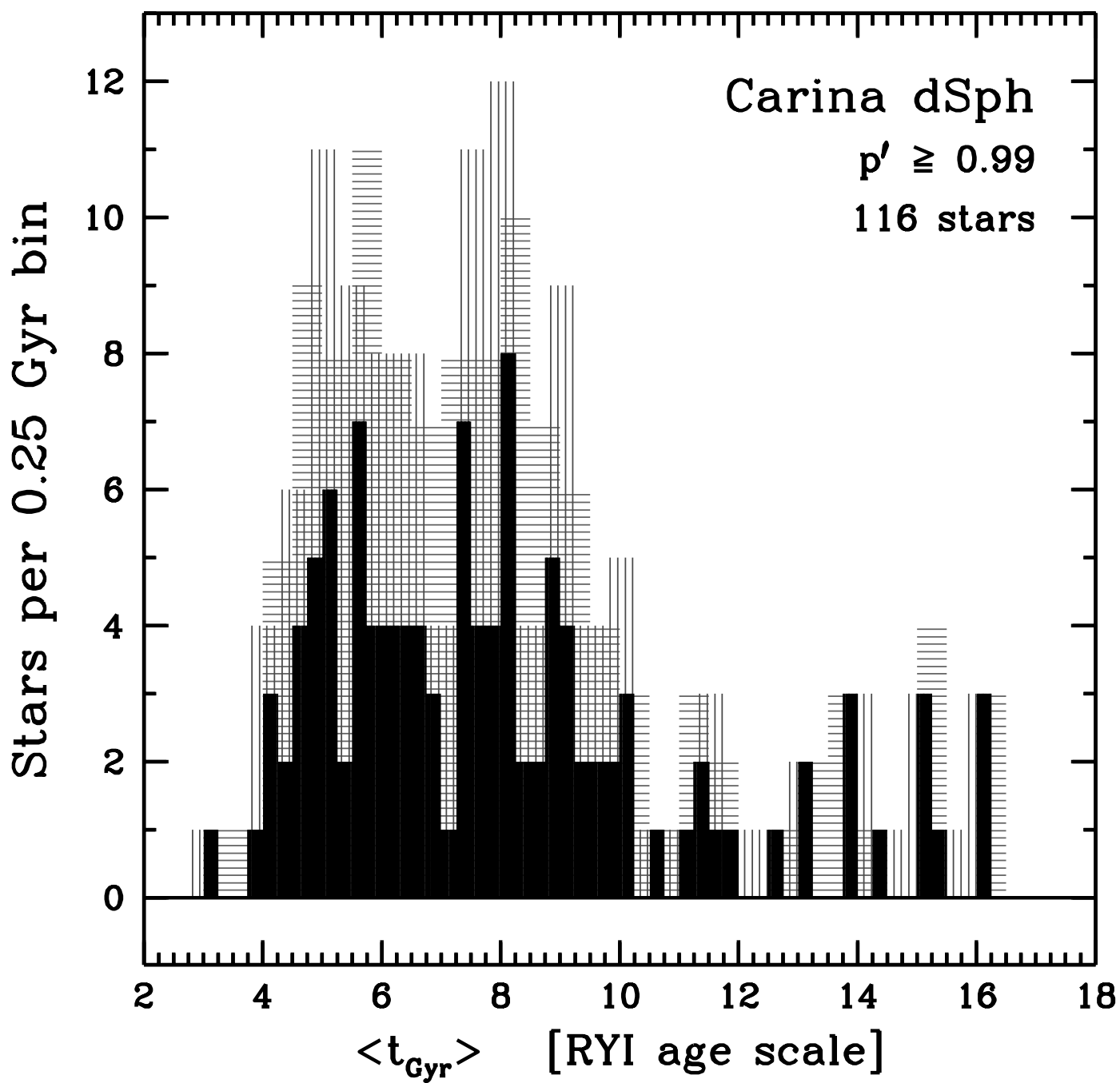


Figure 9 of Mighell (1997)